TIME-LAPSE ACTIVE SOURCE SEISMIC CHARACTERIZATION OF A LEAKY CO_2 RESERVOIR: LITTLE GRAND WASH FAULT, UTAH

by

Stephen Slivicki

A thesis

submitted in partial fulfillment

of the requirements for the degree of

Master of Science in Geophysics

Boise State University

August 2022

BOISE STATE UNIVERSITY GRADUATE COLLEGE

DEFENSE COMMITTEE AND FINAL READING APPROVALS

of the thesis submitted by

Stephen Slivicki

Thesis Title: Time-Lapse Active Source Seismic Characterization of a leaky CO2 Reservoir: Little Grand Wash Fault, Utah

Date of Final Oral Examination: 05 May 2022

The following individuals read and discussed the thesis submitted by student Stephen Slivicki and they evaluated the student's presentation and response to questions during the final oral examination. They found that the student passed the final oral examination.

Lee Liberty, M.S.	Chair, Supervisory Committee
Dylan Mikesell, Ph.D.	Member, Supervisory Committee
Jeffrey Johnson, Ph.D.	Member, Supervisory Committee

The final reading approval of the thesis was granted by Lee Liberty, M.S., Chair of the Supervisory Committee. The thesis was approved by the Graduate College.

DEDICATION

I would like to dedicate this thesis, the culmination of my nine years of higher education, to my parents. They have supported me every step of the way on this journey that started with technical college for welding in 2010 and ended with a master's degree in geophysics over a decade later in 2022. Their love and support are what made this journey possible and are invaluable to me, thank you.

ACKNOWLEDGMENTS

Foremost, I want to give a special thanks to my advisor Lee Liberty who provided me with the opportunity to pursue higher education at Boise State University, and whose guidance and insight along the way were invaluable. I could not have asked for a better academic mentor to study under in pursuit of my master's degree.

In addition, I want to thank my committee members. Dylan Mikesell and Jeffery Johnson for their guidance in my research.

I would also like to acknowledge Tom Otheim, Jonathan Yelton, as well as the UTEP crew that assisted with data collection during our field campaign to Crystal Geyser.

I would also like to especially thank my fellow graduate students Spencer Wilbur and Mitch Creelman who supported me throughout this entire journey, and especially in these last few months as I was writing my thesis and preparing for my defense.

Finally, I would like to thank my friends back home in the Midwest, Lane, Alex, Brandon, and Kale who were my internet lifeline to sanity during the pandemic lockdowns of 2020. True friends indeed!

ABSTRACT

A carbon capture and sequestration (CCS) approach requires economical methods to monitor reservoir CO_2 flow paths through time. I explore the use of an inexpensive surface seismic approach to monitor the time-varying response of a leaky CO_2 reservoir. My site is located in east central Utah, where the Little Grand Wash fault provides a natural analogue for a failed sequestration site. This fault and related anticlinal trap provides a conduit to collect and deliver CO_2 from shallow reservoir depths to the atmosphere. Elevated soil CO_2 flux measurements, outgassing at the Crystal Geyser, and travertine deposits provide the surface expression of CO_2 seeps along and near the fault. Borehole and past geophysical data provide a structural and stratigraphic framework for the site.

Through historic and new water temperature data, I identify and characterize eruption cycles at the Crystal Geyser. I show that the frequency and duration of eruptions changes through time, and I observe an overall increase in eruption duration. With a new seismic monitoring approach, I show that a surface-based accelerated weight drop source into a stationary geophone spread is repeatable and appropriate for time-lapse seismic studies to monitor reservoir changes. I show repeated surface and body wave measurements with a 30-hour time-lapse dataset. I model seismic velocity changes with changing CO_2 saturation within the main Navajo Sandstone reservoir. My models show that during initial saturations, seismically resolvable reservoir changes are possible to monitor. However, I show that a critically saturated reservoir, like that along the Little

Grand Wash fault, shows travel time or amplitude changes that are below the resolving capabilities of my surface-based seismic system. While my surface based seismic approach is not appropriate for monitoring CO_2 changes at my field site, this same approach could be used to monitor CO_2 changes during initial CCS injection where a larger seismic response would be expected.

TABLE OF CONTENTS

DEDICATION iv

ACKNOWLEDGMENTS v

ABSTRACT vi

LIST OF TABLES x

LIST OF FIGURES xi

LIST OF ABBREVIATIONS xv

CHAPTER ONE: INTRODUCTION 1

Motivation and Importance of Research 1

CHAPTER TWO: CRYSTAL GEYSER - ANALOG FOR FAILED CCS SITE 7

Regional Geology 7

Strata of the Little Grand Wash Fault 9

LGWF CO_2 Outgassing History and Sources 10

Supercritical CO_2, Migration and Near Surface Reservoirs 11

Crystal Geyser and Its Eruption Cycles 14

CHAPTER THREE: METHODS AND DATA ACQUISITION 16

Field Acquisition and Data Reduction 16

Eruption Tracking at Crystal Geyser 19

Camera Runtime and Placement 20

CHAPTER FOUR: SEISMIC MODELING 22

PatchyW Model Parameters 22
Zoeppritz Equations 28
CHAPTER FIVE: SEISMIC DATA ANALYSIS 29
Common Offset Phase Picking and Processing 29
Time-lapse Amplitude and Travel Time Assessment 31
Surface Wave Analysis 33
CHAPTER SIX: RESULTS 34
Overview 34
Navajo-sourced Geyser Eruptions Derived from Temperature Data 34
Patchy White Modeling 42
Zoeppritz Modeling 43
First Arrival and Reflection Z-score and Travel Time Residuals 45
Day 1 52
Day 2 53
Day 3 56
Dispersion Analysis 61
CHAPTER SEVEN: DISCUSSION 65
Conclusion 67
REFERENCES 69

LIST OF TABLES

Table 4.1 Fluid properties and other Whites model parameters. 26

Table 4.2 Mineral Properties for the Navajo reservoir 27

Table 4.3 Fluid properties and other White model parameters. 27

Table 6.1 Summary of Crystal Geyser eruptions from this study, Han et al. (2013) and Kampman et al. (2014). 40

LIST OF FIGURES

Figure 1.1 Overview of the carbon sequestration process and potential uses. Figure from (https://watchwire.ai/carbon-capture-utilization-storage-pipe-dream-potential-solution/). 2

Figure 1.2 Overview of methods currently used and being researched to monitor carbon sequestration sites from Jenkins et al. (2015).....3

Figure 2.1 Top: Regional tectonic map of the Paradox basin and the surrounding region from Kampman et al. (2014). Outlined grey area approximates the edge of the Pennsylvanian evaporates that define the basin. Bottom: Primary structural features in the northwest portion of the Paradox basin. Yellow stars mark the locations of CO2 outgassing at the surface as springs or dry leaks.....8

Figure 2.2 Top: CO2 flux measurements across the LGWF along Line 7 from Jung et al. (2014). Bottom: LGWF cross section near Crystal Geyser, modified from Probst et al. (2018). Geology at the top of the cross-section simplified from Doelling et al. (2015). Temperature with depth was calculated with geothermal gradients from nearby water well (Heath et al., 2009). Blue and green arrows represent presumed CO2 migration paths. 13

Figure 2.3 Pressure-temperature phase graph for CO2 from Felix Birkelbach (2022). Blue line is the calculated pressure temperature line based on geothermal gradients from a well (Pan American 1 Salt Wash well) located 16.6km from Crystal Geyser from Heath et al. (2009). Squares are units at hanging wall depths while triangles are at footwall depth.....15

Figure 3.1 Geologic map of the study area that includes the Crystal Geyser and my seismic survey location along line 7 (black box). Red and green circles on the map are CO2 soil flux measurements from Jung et. al. (2014) and Han et al. (2013) respectively. The size of the circle indicates relative CO2 flux with greatest flux measured along the fault. Beige polygons represent tufa deposits left by past CO2-charged brines flowing to the surface. LGWF (black lines); top of Navajo Sandstone contours (red lines).....18

Figure 3.2 Aerial photo from Line 7. Geophones are represented by black circles. Map shows surface water observed while in the field. Bedrock geology simplified from Doelling et al. (2015). LGWF zone shown in yellow. 19

Figure 3.3 Google Earth image of the Crystal geyser showing the Camera placement relative to the Crystal Geyser. HPC1 and HPC2 were the placements on November 6th and 7th respectively. HCP3 was the final location about 17 meters from the geyser at about 30cm above the ground..... 21

Figure 4.1 Sonic log derived from a borehole (API: 4301511138) 3km to the northwest of Crystal Geyser. Black lines are estimated unit depths for the Footwall side of the fault on Line 7. Red lines are the inferred depths of the reflectors seen in Figure 5.1..... 24

Figure 5.1 Common trace or offset gather (111) with a 40 to 240 Hz bandpass filter. Maximum and minimum amplitudes for the reflectors and first arrivals are black and cyan plotted lines. Reflector's "A" and "C" are the same as those seen in Figure 5.3..... 31

Figure 5.2 Sample shot gather that has been summed, filtered and gained showing first arrivals, surface waves, and the two primary reflectors A and C. I show the trace 111 common offset gather at 392.5 m for Day 3 in Figure 5.2. Receiver offsets range from -162.5 to 437.5 m..... 32

Figure 6.1 Map of greater Crystal Geyser area. Green triangle is the location of the MOAB Canyon Field Station relative to the Crystal Geyser (yellow star). Borehole that contains the sonic log seen in Figure 4.1..... 36

Figure 6.2 Field campaign window from Nov 8th to 13th with overnight hours (7pm-7am) shaded in grey. Black and green rectangles are camera recorded eruptions and time-lapse seismic recording windows. Camera captured windows are in orange and unrecorded windows are in red. I interpret D-type eruptions overnight on Nov 9th and 12th and B-type eruptions mid-day on Nov 8th and early morning on the 11th. 37

Figure 6.3 30-day Temperature record from November 5th – December 5th 2020 with overnight hour (7pm-7am) shaded in gray. Well head transducer shown in dark blue, air temperature from MOAB weather station shown in red and the Green River water temperature shown in light blue. 38

Figure 6.4 Probability mass function histograms showing temperature distributions of river water (light blue), transducer (dark blue) and air (red) over the 30-day recording window. Left figure shows raw continuous data. Right figure shows daily temperature change which is the difference between daily minimum and maximin values..... 39

Figure 6.5 Modified from Kampman et al. (2014), showing Navajo sandstone-derived geyser eruptions from past studies and during our November 2020 campaign. 41

Figure 6.6 Plot showing how D-type eruption as a percentage of eruption cycle has changed over the last 15 years. 41

Figure 6.7 Graph showing change in Vp within the Navajo sandstone from my Patchy model. Here, I use a baseline of 3600 m/s that represents Navajo Sandstone. 43

Figure 6.8 Graph showing percent change in the reflection coefficient with changing gas percentage as a function of offset (meters) and reflection angle. 45

Figure 6.9 Common offset gather of trace 87 (Offset 277.5m) on Day 1 showing wind noise primarily from 0-175 minutes and another band around 240 minutes.....48

Figure 6.10: Common offset gather of channel 1 on day 2. Black arrows indicate where plate resets can be easily seen in the seismic data due to a shift in travel time. Light blue line in the first arrivals represents peak amplitude pick..49

Figure 6.11 Common offset gather of channel 1 on day 2. Black arrows indicate where plate resets can be easily seen in the seismic data due to a shift in travel time. Light blue line in the first arrivals represents peak amplitude pick..50

Figure 6.12 Common offset gather of channel one on day three. Black arrows indicate where plate resets can be easily seen in the seismic data due to a shift in travel time. Green arrow denotes a shift in travel time from source settling noted on field notes. 51

Figure 6.13 Top: Tomographic velocity model along line 7 by Yelton (2021) with red lines denoting fault zone. Center: first arrival amplitude Z-score during day one with back horizontal lines representing source skips/resets. Vertical red lines denote the fault zone identified by Yelton (2021). Right: Plot of transducer data for day one time lapse window.....53

Figure 6.14 Top: Tomographic velocity model along line 7 by Yelton (2021) with red lines denoting fault zone. Center: Plot of first arrival amplitude Z-score during day two. Black horizontal lines represent source skips and black arrows on y-axis denote source resets. Vertical red lines denote the fault zone identified by Yelton (2021). Right: Plot of transducer data for day two timelapse window. 55

Figure 6.15 Top: Tomographic velocity model along line 7 by Yelton (2021) with red lines denoting fault zone. Center: Plot of first arrival travel time residual during day two with back horizontal lines representing source skips/resets. Right: Plot of transducer data for day two timelapse window. Vertical red lines denote the fault zone identified by Yelton (2021). 56

Figure 6.16 Top: Tomographic velocity model along line 7 by Yelton (2021). Center: Plot of first arrival amplitude Z-score during day three. Black horizontal lines representing source timing skips and black arrows are plate resets . Right: Plot of transducer data for day three timelapse window. Vertical red lines denote the fault zone identified by Yelton (2021). Left: A Crystal geyser eruption was recorded at 12:30 by the hunting camera at the peak temperature and a long-term D-type eruption begins just before 18:00. .. 58

Figure 6.17 Z-scores for reflector "A" over all three days. Black vertical lines denote the skips/resets. White offsets were noisy or unable to be picked..... 59

Figure 6.18 Z-scores for reflector "C" over all three days. Black vertical lines denote the skips/resets. White offset were noisy or unable to be picked. 60

Figure 6.19 Dispersion curves of the first 5 shots on day two for the hanging wall (left) and the footwall (right) of the LGWF. Black lines denote frequencies examined over my time-lapse window in Figure (6.20) 63

Figure 6.20 Dispersion curve time-lapse for 15 Hz (top) and 10 Hz (bottom) across Day one (left) and Day two (left)..... 64

LIST OF ABBREVIATIONS

BSU	Boise State University
MST	Mountain Standard Time
LGWF	Little Grand Wash Fault
CO_2	Carbon dioxide
CCS	Carbon Sequestration site
3-D	Three dimensional

CHAPTER ONE: INTRODUCTION

Motivation and Importance of Research

Mitigating climate change is one of the foremost challenges facing the global community today. The cause of anthropogenic climate change is primarily the release of carbon dioxide (CO_2) into the atmosphere from human activity. Today, CO_2 accounts for about 77% of greenhouse gases in the atmosphere and currently exists in concentrations higher than any other point in the past 800,000 years (Rahman et al., 2017, Lindsey, 2022). Recognizing this threat, the Paris Climate Agreement suggested limiting warming to below two degrees Celsius (dC) globally to avoid the greatest impacts of climate change (Kelemen et al., 2019). In order to achieve this goal, methods to limit CO_2 emissions and/or extracting CO_2 from the atmosphere are needed.

One method to reduce CO_2 emissions includes a carbon capture and sequestration (CCS) approach (Figure 1.1). At CCS sites, CO_2 emissions from large industrial point sources, such as power plants, are captured and pumped into underground reservoirs for long term storage. The CO_2 that can be contained at these sites could limit warming to below the threshold called for by the Paris agreement (Kelemen et al., 2019). Pilot CCS projects have been initiated at sites such as Frio-II pilot site in southeast Texas (Zhu et al., 2019), Sleipner in the Norwegian North Sea (Williams and Chadwick 2012), and Ketzin, Germany (Boullenger et al., 2015).

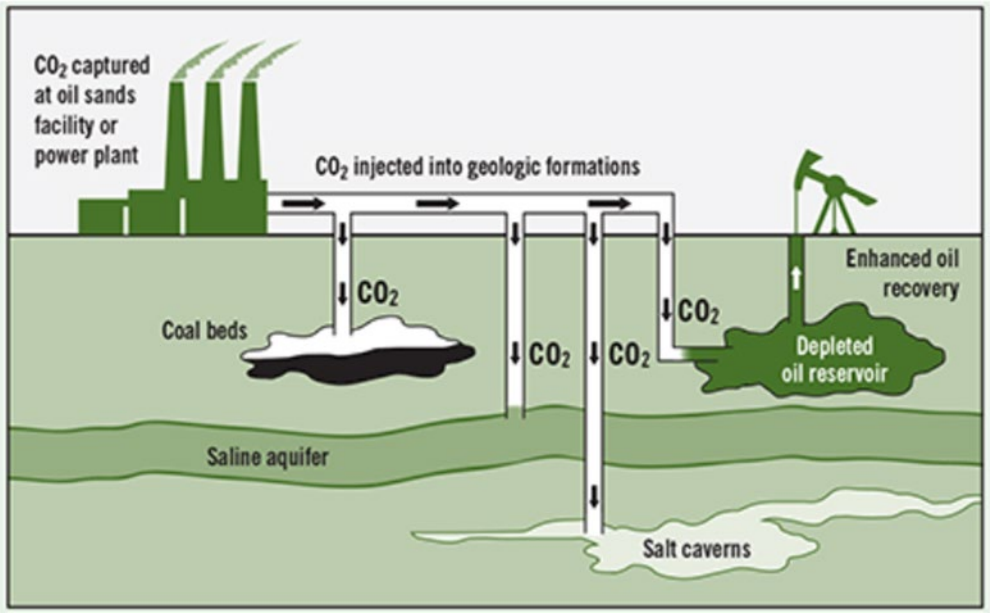

Figure 1.1 Overview of the carbon sequestration process and potential uses. Figure from (https://watchwire.ai/carbon-capture-utilization-storage-pipe-dream-potential-solution/).

CCS success depends on an accurate assessment and characterization of both reservoirs and geologic boundaries to trap CO_2 within the reservoir. Understanding how existing faults and other fluid-permeable pathways influence CO_2 migration in the subsurface is vital. Relevant questions are: 1. How does CO_2 migrate through porous reservoirs at varying time scales? 2. How does CO_2 migrate along high permeability pathways (e.g., faults) that may overlie a CCS site at similar time scales? And 3. What methods are available to monitor CO_2 -charged fluids or gas movement?

Methods to monitor subsurface CO_2 at CCS sites are needed at many time scales. Monitoring should not only track CO_2 movement and potential leakage points but should also consider caprock integrity to assess the potential for groundwater contamination and atmospheric CO_2 releases (Kelemen et al., 2019). A few methods of monitoring CCS sites that have been explored and include pressure variation monitoring, interferometric synthetic aperture radar and seismic imaging (Kelemen et al., 2019). The most favored

of these is methods is the use of seismic imaging techniques. Several studies have assessed the use of ambient-noise seismic interferometry (Kelemen et al., 2019), time-lapse seismic imaging (Williams and Chadwick 2012, Boullenger et al., 2015) and seismic coda waves to monitor subsurface CO_2 with varying success (Zhu et al., 2019; Figure 1.2). Additionally, multi-year 3-D timelapse seismic monitoring is already in use as a compliance method at several sites (Jenkins et al., 2015).

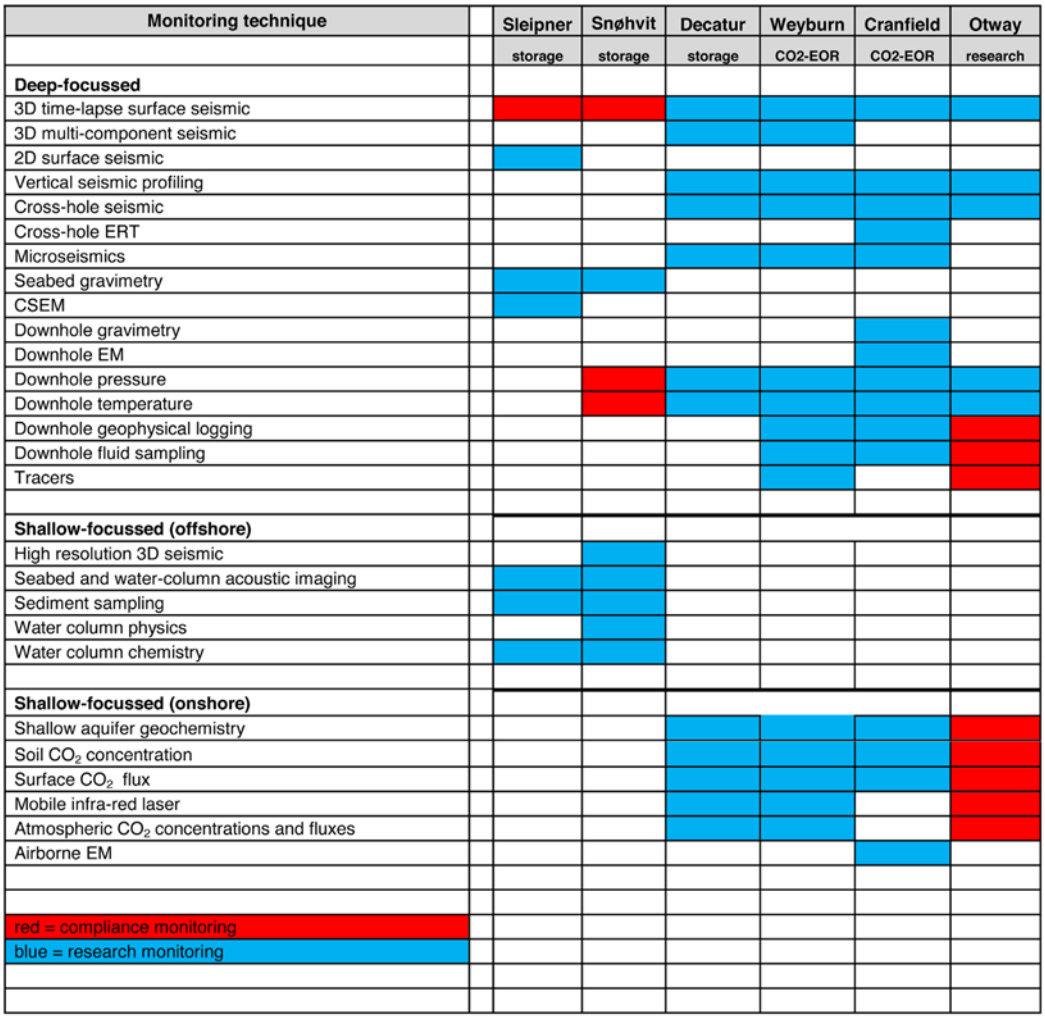

Monitoring technique	Sleipner	Snøhvit	Decatur	Weyburn	Cranfield	Otway
	storage	storage	storage	CO2-EOR	CO2-EOR	research
Deep-focussed						
3D time-lapse surface seismic						
3D multi-component seismic						
2D surface seismic						
Vertical seismic profiling						
Cross-hole seismic						
Cross-hole ERT						
Microseismics						
Seabed gravimetry						
CSEM						
Downhole gravimetry						
Downhole EM						
Downhole pressure						
Downhole temperature						
Downhole geophysical logging						
Downhole fluid sampling						
Tracers						
Shallow-focussed (offshore)						
High resolution 3D seismic						
Seabed and water-column acoustic imaging						
Sediment sampling						
Water column physics						
Water column chemistry						
Shallow-focussed (onshore)						
Shallow aquifer geochemistry						
Soil CO_2 concentration						
Surface CO_2 flux						
Mobile infra-red laser						
Atmospheric CO_2 concentrations and fluxes						
Airborne EM						
red = compliance monitoring						
blue = research monitoring						

Figure 1.2 Overview of methods currently used and being researched to monitor carbon sequestration sites from Jenkins et al. (2015).

To date, surface-based seismic approaches have mostly monitored CO_2 reservoir changes on annual or longer time scales through repeat 2-D and 3-D seismic surveys from baseline surveys. Short-duration, surface-based monitoring using established approaches is not practical, as these surveys are expensive and can take many weeks to acquire. Observations at shorter time scales have been conducted with the use of downhole seismic measurements in monitoring wells to monitor active injection. (e.g., Zhu et al., 2019). However, these tests are also expensive and are limited to borehole locations. To accommodate these limitations, I explore the use of a low-cost surface based time-lapse seismology approach to track changes in subsurface CO_2 over the span of hours to days using a fixed weight drop source and geophone receiver survey. I explore this approach because it is a cheaper alternative to borehole seismic surveys, as it requires minimal interactions with a field crew and little time to instrument. I show that while this approach only samples a small portion of the seismic wavefield, fluid-to-gas exchanges at known reservoir depths and within the overlying shallow permeable pathways can be jointly assessed in near real-time. Travel paths between source and receiver can be modeled prior to a time-lapse experiment. Then through rock physics relationships, changing properties along these same ray paths can be identified through seismic amplitude and travel time measurements. From a newly acquired dataset, I explore the limits and capabilities of this approach. I estimate fluid and gas changes in the subsurface through both borehole and surface measurements at a site where CO_2 outgasses at the surface akin to a failed CCS site (e.g., Kampman et al., 2014).

In November of 2020, a Boise state team helped me acquire 30 hours of active source time-lapse seismic data. We deployed geophones across the Little Grand Wash

Fault (LGWF), east central Utah, to explore changing surface and body wave signals related to CO_2 migration and outgassing. The LGWF bisects the Green River anticline, a known CO_2 pathway that delivers CO_2 to the surface from reservoir depths (Jung et al., 2014). I compare changing seismic signals to eruption cycles at the nearby and fault-controlled Crystal Geyser borehole using water temperature data and observed groundwater eruptions.

I address the following questions: 1) How is the eruption cycle of the Crystal Geyser changing through time and do these changes represent a local or regional cycle of CO_2 outgassing; 2) What is the repeatability of my seismic survey on a scale of minutes to hours; 3) Can I monitor subsurface changes in gas saturation base time-lapse seismic record at the LGWF site; and 4) Can I apply this approach to other CCS sites?

To answer these questions, I compare eruption characteristics during a 30-day window to past measurements. I also develop physical property models for my field site by applying rock physics relationships established from other studies. I then focus on field-based measurements to observe travel time and amplitude changes from the top of a CO_2 charged reservoir and within a high permeability fault that directly delivers CO_2 to the atmosphere (Yelton, 2021).

Chapter One of this thesis outlines seismic and non-seismic methods that have been previously used to monitor subsurface CO2 migration through a high porosity reservoir and through shallow permeable pathways. In Chapter Two, I describe the geologic and tectonic framework for the LGWF system and highlight the CO2-charged systems of east-central Utah. I then showcase the strength of my particular approach and why my study area is an ideal place to test my monitoring approach in Chapter Three. In

Chapter Four, I give an overview of the patchy saturation model and Zoeppritz equations that I use to predict how seismic properties change with gas saturation. In Chapter Five, I describe the processing workflow for both static and time-lapse seismic data. In the first part of Chapter Six, I discuss the identification of Crystal Geyser eruptions in the transducer record and show the results of seismic modeling. In the latter portion of Chapter Six, I describe sources of temporal seismic change and identify the changes they cause in processed time-lapse seismic data. Finally, in Chapter Seven I discuss the significance of my findings in the context of the Crystal Geyser, and how these methods could be applied to other CCS sites.

CHAPTER TWO: CRYSTAL GEYSER - ANALOG FOR FAILED CCS SITE

Regional Geology

The Paradox Basin, centered in southeastern Utah, is an oblong shaped tectonic down warp that evolved primarily during the Pennsylvanian and Permian period (Figure 2.1). The basin accumulated deposits of organic rich shale, carbonates, halite and clastics (Nuccio et al.,1996) . The basin was shaped by the Laramide orogeny that uplifted the Colorado Plateau. This deformation resulted in a complex series of northwest-trending folds and faults throughout the basin that were later incised by rivers such as the Colorado and Green Rivers (Nuccio et al., 1996).

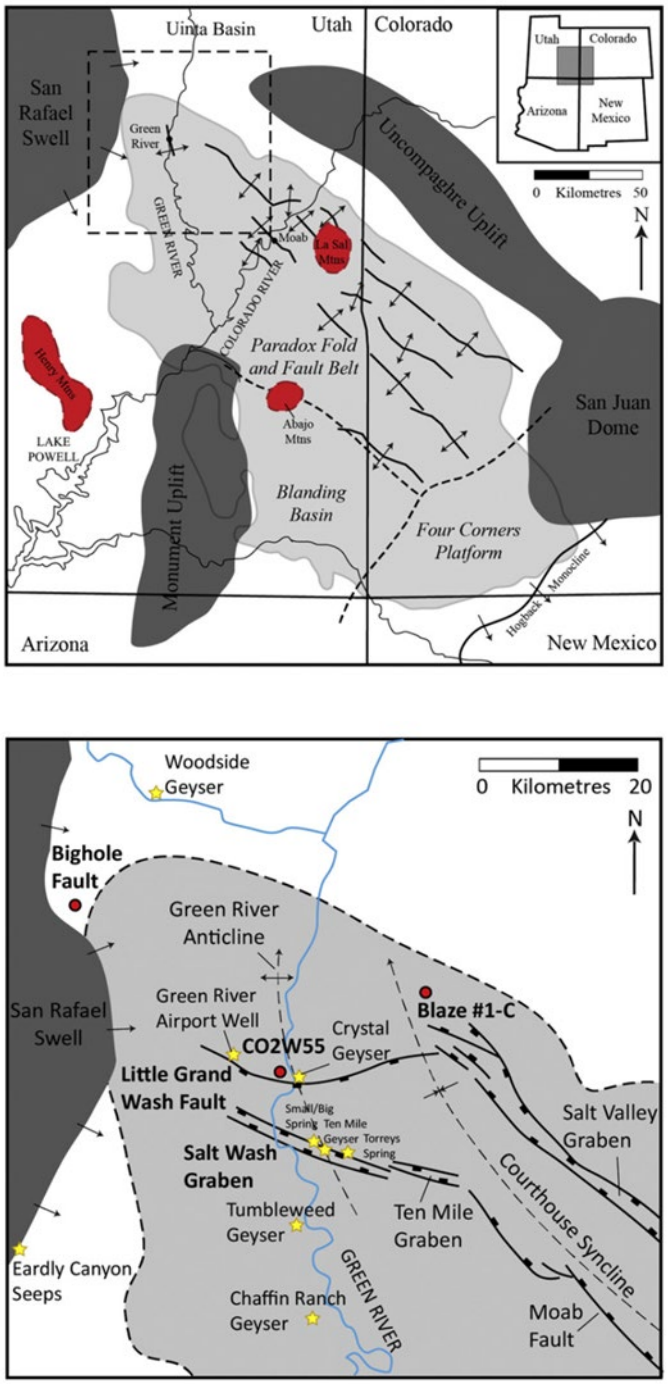

Figure 2.1 Top: Regional tectonic map of the Paradox basin and the surrounding region from Kampman et al. (2014). Outlined grey area approximates the edge of the Pennsylvanian evaporates that define the basin. Bottom: Primary structural features in the northwest portion of the Paradox basin. Yellow stars mark the locations of CO2 outgassing at the surface as springs or dry leaks.

The area of interest for this study is in the northwestern extent of the Paradox basin near the Crystal Geyser (Figure 2.1). Here, the north-plunging Green River anticline is segmented by the east/west-trending LGWF (Shipton et al., 2004). The 61-km long fault dips roughly 70 degrees to the southeast (Shipton et al., 2004; Yelton, 2021). The fault splays into two strands near the Green River where an estimated 200 to 300 m of displacement is focused mostly on the southern segment (Oye et al., 2021; Shipton et al., 2004; Yelton, 2021). The fault's damage zone was initially estimated at 20-30 meters wide, but a recent geophysical study suggested that the damage zone is closer to 60 m wide (Dockrill & Shipton, 2010; Yelton, 2021). The LGWF cuts through a series of gently north dipping interlayered reservoir-seal units that are Jurassic to Cretaceous in age (Dockrill & Shipton, 2010). Age of slip activity along the LGWF is poorly constrained but continued low-slip motion is inferred from moderate magnitude regional earthquakes (Han et al., 2013, Shipton et al., 2004).

Strata of the Little Grand Wash Fault

At the surface on the footwall (north) side of the LGWF at my research site, low permeability shallow marine sandstone, shale and gypsum layers of the Summerville formation are exposed, and cap the reservoir sandstones of the Entrada Formation (Kampman et al., 2014; Figure 2.2). Below the 150 m thick Entrada unit, the low permeability 50 m thick Carmel formation is mapped and is comprised of shale, gypsum and siltstone layers. This unit acts as a seal to the overlying Entrada and underlying Navajo sandstone reservoirs (Kampman et al., 2014). At my site, the 100 m thick Navajo sandstone overlies the weakly permeable Kayenta Formation, and acts as a sealing unit to the underlying Wingate reservoir (Kampman et al., 2014). On the hanging wall (south)

side of the LGWF, the Mancos Shale is exposed at the surface and has a depth of about 250m before transitioning to the Summerville and deeper formations described above (Kampman et al., 2014).

The offset of the LGWF near my study area places the Entrada and Navajo sandstone reservoir units against shales, siltstones, and other sandstones (Kampman et al., 2014). Previous studies concluded that the fault geometry and related lithology seals the LGWF from lateral CO_2 flow, but the fault promotes the vertical flow of CO_2 to the surface (Dockrill & Shipton, 2010).

LGWF CO_2 Outgassing History and Sources

The Paradox basin is home to several large CO_2 reservoirs that have been tapped for a number of industrial uses (Han et al., 2013). While much of the CO_2 remains in these reservoirs, there are several localities, such as the LGWF, where CO_2 migrates to the surface. This is evidenced by travertine deposits in the area which date to 400ka near the Salt Wash Graben to the south and 100ka within the Green River anticline near Crystal Geyser (Burnside et al., 2013). The CO_2 leakage points along the fault vary both spatially and temporally, possibly due to fracture sealing and formation caused by earthquakes, carbonate precipitation, or other changes in reservoir conditions (Han et al., 2013).

The initial source of CO_2 is still poorly understood, and several theories have been suggested including chemical reactions between the Navajo Sandstone and ground water (Baer and Rigby, 1978), exsolution from brine in the Navajo Sandstone and thermal decomposition of carbonate rocks (Mayo et al., 1991). Heath et al. (2009) suggested that the origin of CO_2 may be a combination of clay-carbonate reactions and

thermal decomposition of carbonates at depths greater than 800 m. Wilkinson et al. (2009) concluded that upwards of 20% of the CO_2 emitted from the Crystal Geyser originates from the mantle. This conclusion is based on helium, neon, argon, krypton, and carbon isotope analysis. Interestingly, analysis of the gasses emitted from other nearby geysers show a greater fraction, 16-99%, originating from the mantle, suggesting that sources may vary across the Paradox basin (Wilkinson et al., 2009, Han et al., 2013). In short, at least a portion of the CO_2 originates at depths of greater than 800m, but the exact source origin is unclear (Han et al., 2013). The CO_2 source is not relevant to my study.

Supercritical CO_2, Migration and Near Surface Reservoirs

The LGWF, while laterally sealing, provides vertical pathways for the migration of CO_2 from depth within the Green River anticlinal trap (Jung et al., 2015, Kampman et al., 2014). CO_2 was found in a supercritical state at depths greater than 800m from oil explorations in the area. The CO_2 transitions to a gas as it migrates to the surface along the LGWF (Kampman et al., 2014). The phase transition from supercritical to liquid, based on temperature and pressure regimes, is approximated at about 700m depth (Heath et al., 2009; Figure 2.3). Here, I focus on depths of less than 300m, where CO_2 presumably exists only in a gas phase.

As CO_2 migrates upwards along the LGWF, the gas charges the near surface Entrada, Navajo, and Wingate sandstone reservoirs with CO_2 brine and gas (Jung et al., 2014, Kampman et al., 2014). The brine then mixes with the meteoric waters that originate from the San Rafael Swell before outgassing as CO_2 springs or geysers (Jung et al., 2015, Jung et al., 2014, Kampman et al., 2014; Figure 2.3). These observations, along with temperature, chemical and microbial community studies of Probst et al. (2018)

confirm that CO_2 is passing through the reservoir from depth and is released to the atmosphere. Scientific borehole CO2W55, located 1.5 km to the west of my study area, drilled into the foot wall of the LGWF (Figure 2.1) found brine charged with dissolved CO_2 within the Navajo Sandstone reservoir at a depth of 200-290m, but no free CO_2 gas (Kampman et al., 2014). CO2W55 did host pockets of free CO_2 gas within the Entrada sandstone at a depth of 50-140m (Kampman et al., 2014). Based on the findings of CO2W55, Kampman et al. (2014) suggested that the CO_2 brine degasses within the LGWF and shallow reservoirs before outgassing at the surface.

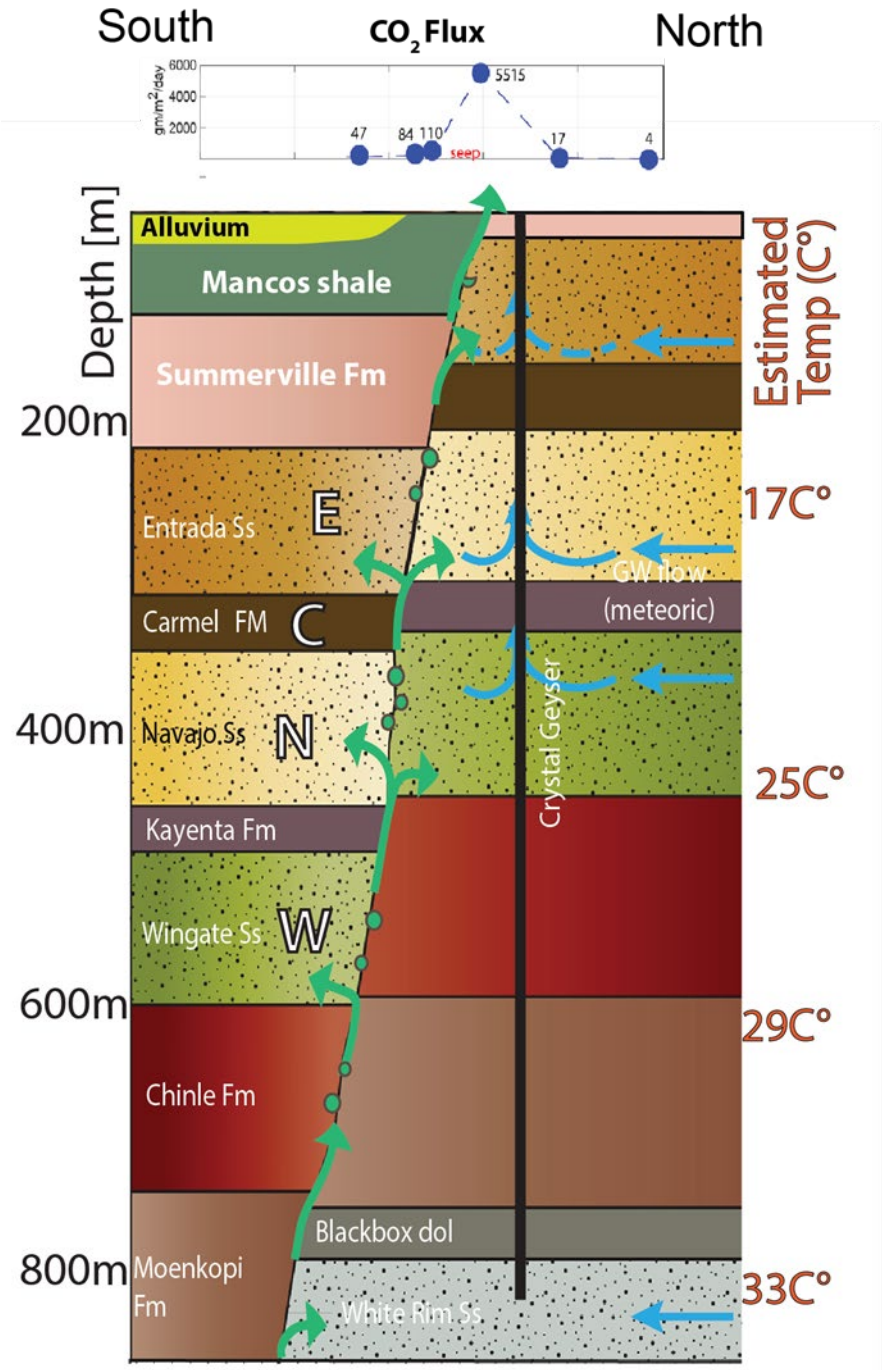

Figure 2.2 Top: CO2 flux measurements across the LGWF along Line 7 from Jung et al. (2014). Bottom: LGWF cross section near Crystal Geyser, modified from Probst et al. (2018). Geology at the top of the cross-section simplified from Doelling et al. (2015). Temperature with depth was calculated with geothermal gradients from nearby water well (Heath et al., 2009). Blue and green arrows represent presumed CO2 migration paths.

Crystal Geyser and Its Eruption Cycles

The Crystal Geyser, drilled in 1935, was a hydrocarbon exploration well located along the LGWF and adjacent to the Green River (Han et al., 2013; Figure 3.1). This well, drilled through the Green River anticline to a depth of 800m, was abandoned due to abnormally high fluid pressures (Han et al., 2013). CO_2-charged eruptions continue each day through the original drill pipe. The eruptions, based on water temperature and microbial constituents, are classified as A through D type (Han et al., 2013, Probst et al., 2018). Each eruption type contains a unique duration and repeat time (Han et al., 2013). The duration and recharge interval of these eruption types has evolved considerably over the past decade (Kampman et al., 2014). Based on the water temperature of about 16.9°C during both B- and D-type eruptions, Heath et al. (2009) suggested that the related CO_2 source was from the Navajo sandstone. This temperature matches the Navajo Sandstone reservoir temperature along the LGWF and is consistent with the measured geothermal gradient of the region (Utah Geological Survey, 2012, Heath et al., 2009). The primary difference between B- and D-type eruptions is that B-type eruptions are considerably shorter in duration and recharge interval compared to D-type eruptions (Han et al., 2013; Kampman et al., 2014). To provide modern eruption characteristics, I quantify eruptions at the Crystal Geyser using transducers to record eruption timing and temperature over a 30-day window.

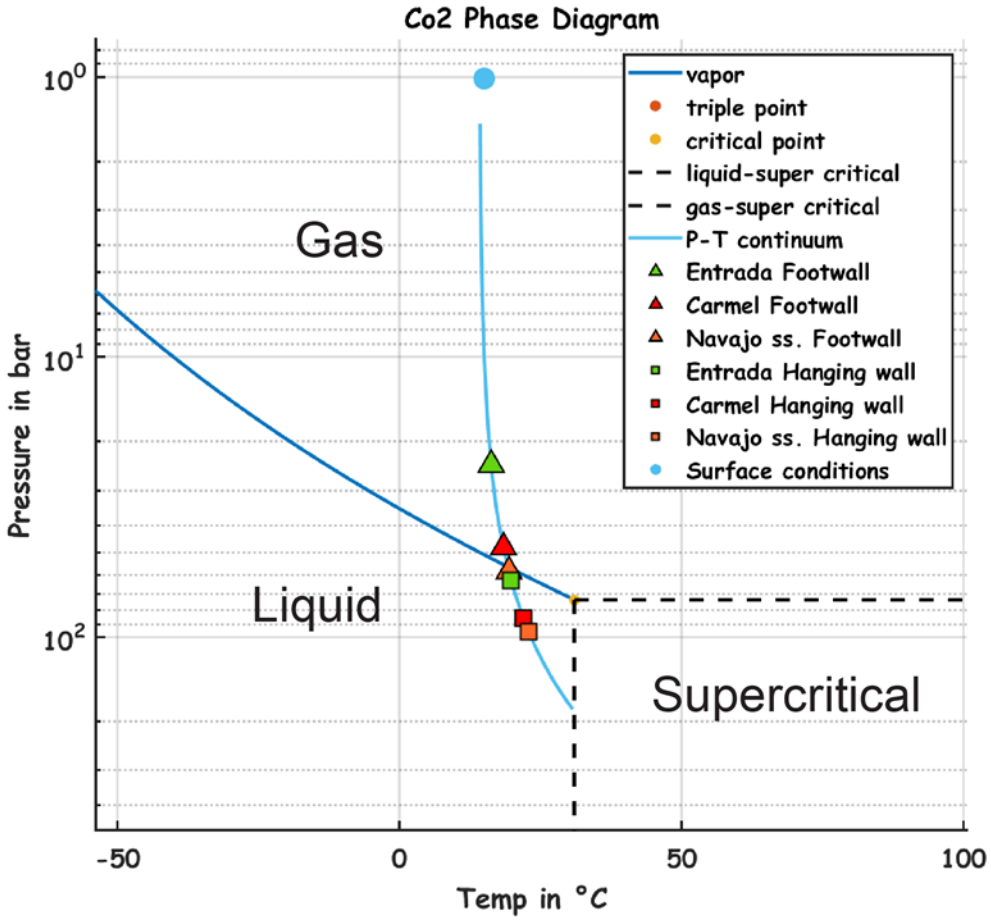

Figure 2.3 Pressure-temperature phase graph for CO2 from Felix Birkelbach (2022). Blue line is the calculated pressure temperature line based on geothermal gradients from a well (Pan American 1 Salt Wash well) located 16.6km from Crystal Geyser from Heath et al. (2009). Squares are units at hanging wall depths while triangles are at footwall depth.

CHAPTER THREE: METHODS AND DATA ACQUISITION

Field Acquisition and Data Reduction

To explore whether CO_2 flux measurements relate to changing gas content within a reservoir or fault system, I examine time-lapse seismic data. Seismic data acquisition was carried out by the Boise State team during a November 2020 field campaign. This followed two campaigns in 2019 and 2020 where seven active source profiles were acquired (Yelton, 2021). The focus of my survey was along Line 7, approximately two km east of the Crystal Geyser (Figure 3.1). This profile follows a natural drainage where the highest natural CO_2 flux values were regionally measured (Jung et al., 2014; Figure 3.1).

The active source survey was acquired along the northeast-trending Line 7 with 120, 10-Hz vertical geophones, spaced 5 meters apart (Figure 3.1). Line 7 crosses the LGWF between geophone 50 and 70 (Yelton, 2021; Figure 3.2). The northern footwall of the LGWF extends between geophones 80 and 120, and lies above a drainage at the base of a canyon wall, with a 90m difference from the bottom to the surrounding cliffs. Sandstone of the Summerville formation is exposed along the canyon (Doelling et al., 2015) and extends to about 50m below ground. Below the Summerville Formation, the Entrada sandstone reservoir is identified from nearby borehole logs (API: 43-019-11521). Between geophone 51 and 66, the deployment team noted standing water that pools at the surface (Figure 3.2). Here, active gas bubbling was observed, and high CO_2 flux measurements were measured (Jung et al., 2014). CO_2 flux measurements range from

16.7 to 5517.4 gm/m^2, the latter of which is the highest regional flux measurements found outside of Crystal Geyser. Between geophone 1 and 46, deeply weathered shales of the Mancos Formation with overlying Quaternary alluvial deposits are mapped by Doelling et al. (2015) within the hanging wall block of the LGWF.

The source for this survey was a 200 kg accelerated weight drop placed between geophone 30 and 31, along the Crystal Geyser access road (Figure 3.2). The source was programmed to hit the ground every 30 seconds. We sampled each record at one millisecond and recorded for 10 seconds. We acquired the data over three, 10-hour daylight windows. Geophones remained in the ground for the entire survey to minimize acquisition-based signal changes.

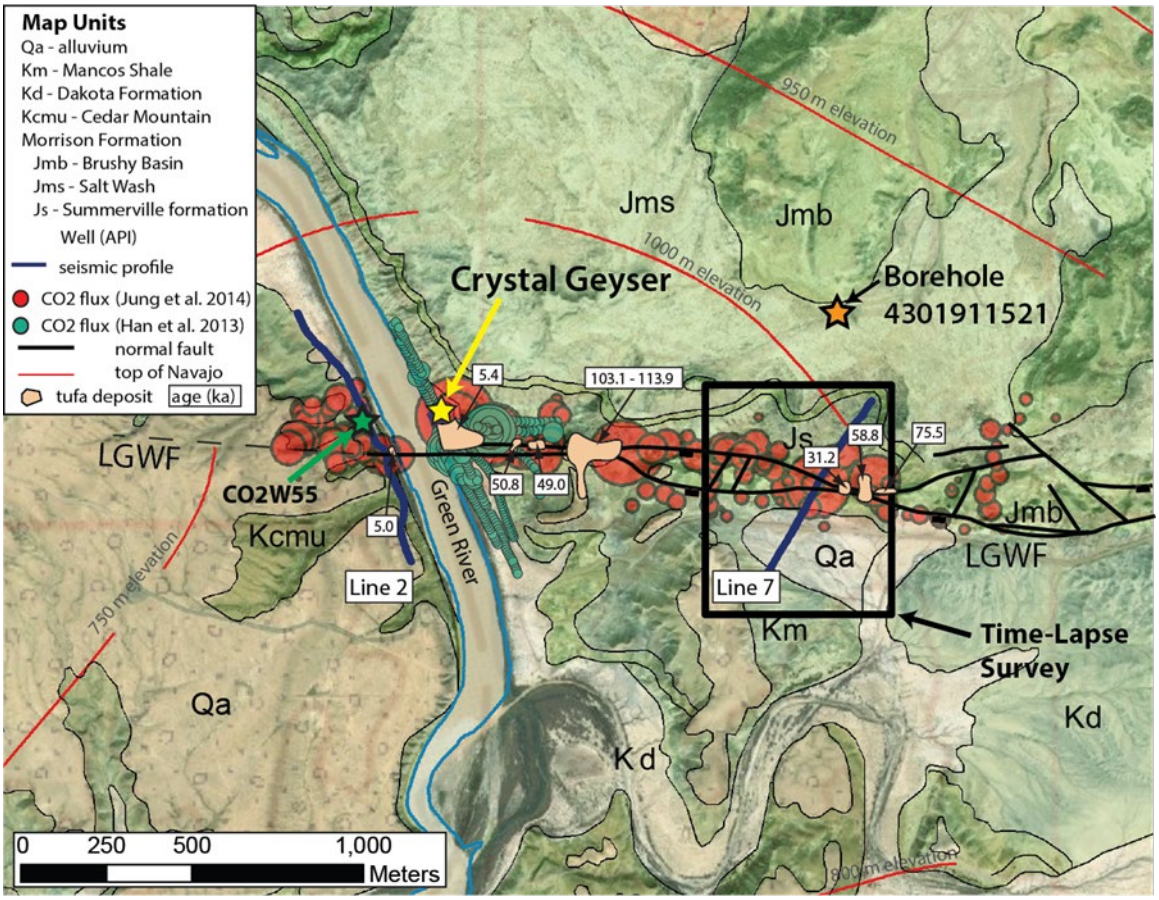

Figure 3.1 Geologic map of the study area that includes the Crystal Geyser and my seismic survey location along line 7 (black box). Red and green circles on the map are CO2 soil flux measurements from Jung et. al. (2014) and Han et al. (2013) respectively. The size of the circle indicates relative CO2 flux with greatest flux measured along the fault. Beige polygons represent tufa deposits left by past CO2-charged brines flowing to the surface. LGWF (black lines); top of Navajo Sandstone contours (red lines).

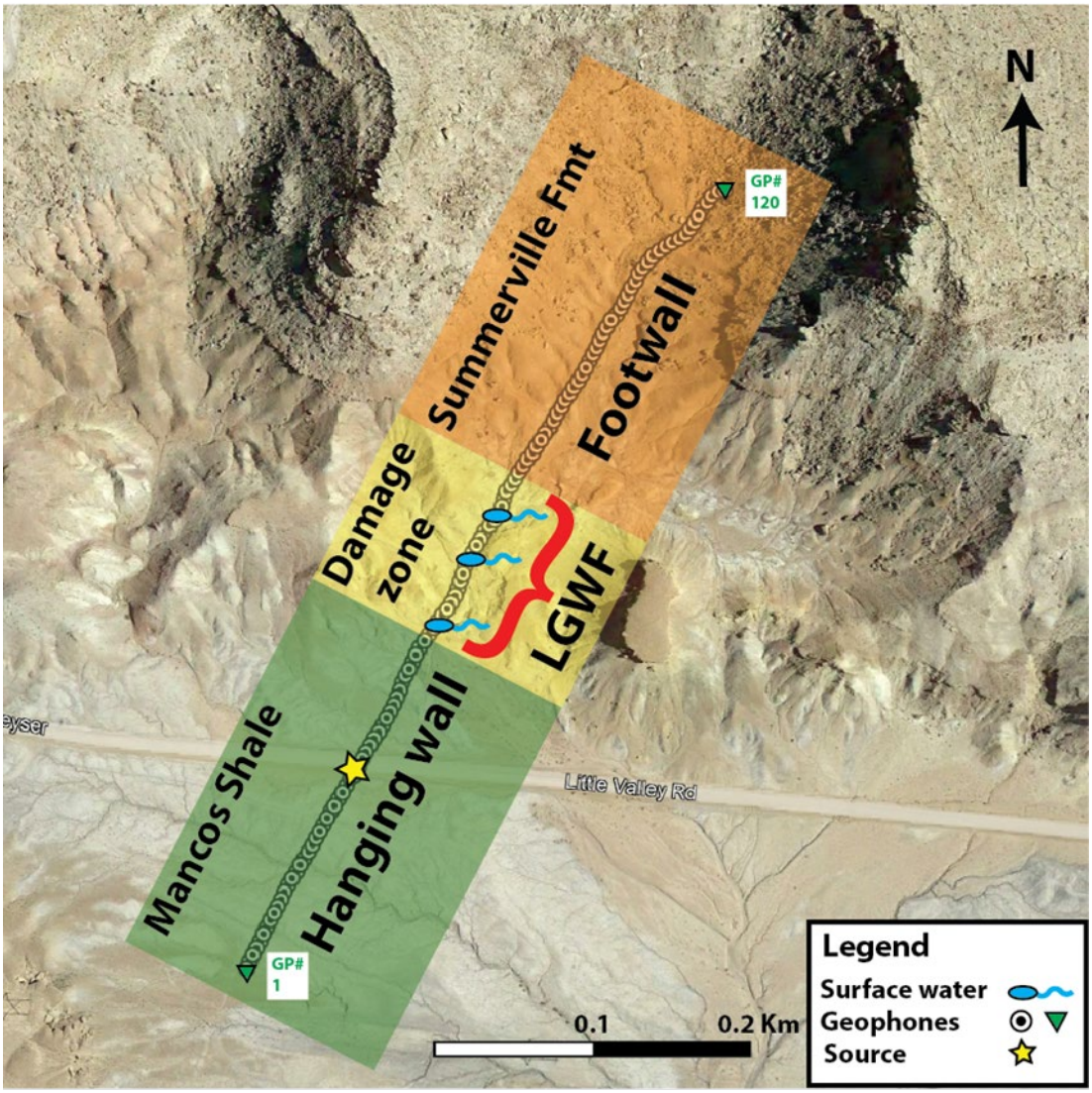

Figure 3.2 Aerial photo from Line 7. Geophones are represented by black circles. Map shows surface water observed while in the field. Bedrock geology simplified from Doelling et al. (2015). LGWF zone shown in yellow.

Eruption Tracking at Crystal Geyser

To compare my seismic measurements to eruption cycles, the Boise State team deployed two pressure transducers that recorded hydrostatic pressure and temperature at the Crystal Geyser borehole (Figure 3.1). One sensor was attached to the outside well casing to record air temperature between eruptions, water temperature during eruptions as it flowed over the borehole casing, and barometric pressure. This sensor (Hobo C8

10571120) was placed 0.14 m below the top of casing. The second transducer (Hobo C8 10751151) was placed within the casing at a depth of 1.66 meters below the well head that measured 1.4 m above the ground surface. The depth to the second transducer was slightly above static water level between eruptions. The ground elevation at the Crystal Geyser measured about 8.5 m above the elevation of the Green River that lies about 60 m to the west. These instruments recorded at a two-minute sample rate, beginning at 8:00 am Mountain Standard time (MST) November 05, 2020, through 11:00 am MST December 05, 2020. Unfortunately, during the 30-day recording window, the downhole transducer was lost, and no data was recovered. However, the top-of-casing sensor remained intact, and a robust temperature dataset was exploited. In Chapter Six, I examine the one temperature dataset and compare my observations with previously published results.

Camera Runtime and Placement

I deployed a motion-activated camera at the Crystal Geyser to capture video of the geyser eruption cycles during the seismic survey. The camera was placed in two locations before finding its final ideal placement on vegetation to the south of the geyser at HCP3 (Figure 3.3). From November 6th through November 8th, the camera had a number of issues such as battery failure and blockage by vegetation. After the 9th, when an external battery was left with the camera, it continuously recorded until 11:48:00 MST on November 12th. The video capture function was used to record eruptions at 10 frames per second in 1080p and captured sound. The camera trigger was set to “Instant”, meaning that as soon as the camera detected motion beyond a certain threshold it recorded video of the Crystal Geyser. The threshold was consistently triggered by

eruptions of about one foot in height or greater over the well head. I captured eruptions during five vigorous geyser eruptions that averaged in height from 0.3 -1 meters.

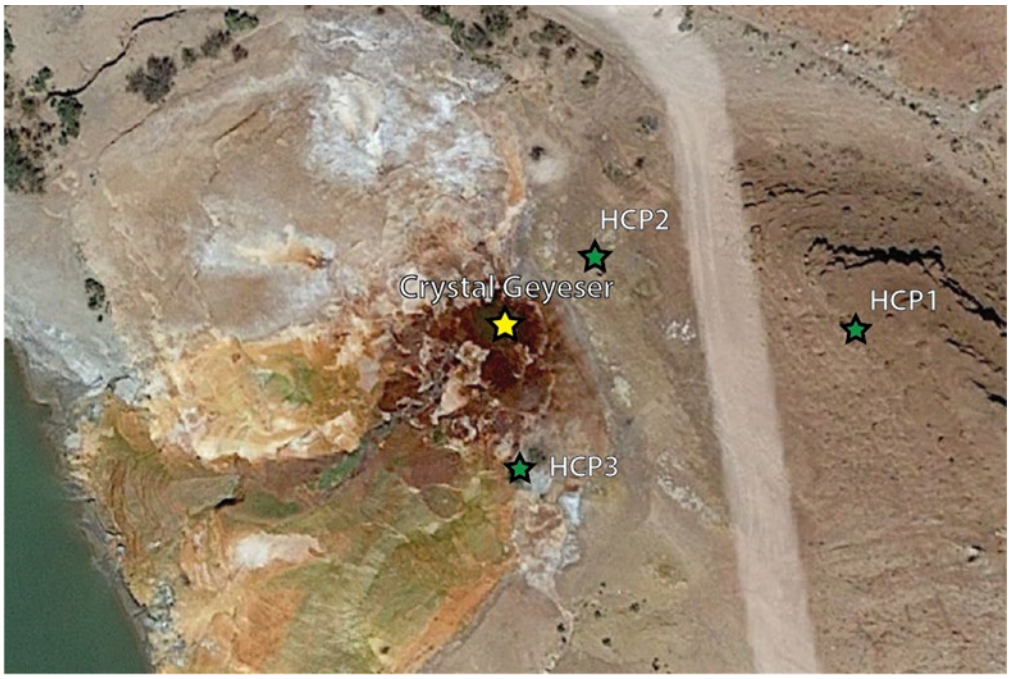

Figure 3.3 Google Earth image of the Crystal geyser showing the Camera placement relative to the Crystal Geyser. HPC1 and HPC2 were the placements on November 6th and 7th respectively. HCP3 was the final location about 17 meters from the geyser at about 30cm above the ground.

CHAPTER FOUR: SEISMIC MODELING

PatchyW Model Parameters

Gassmann (1951) developed a relationship that relates the bulk modulus of a rock to its pore, frame and fluid properties. However, Gassmann (1951) only accounted for a single homogenous saturating fluid and not multiple phases. White (1975) expanded on Gassmann's relationships to account for mixed or "patchy" saturations of liquids, such as gas and water which can cause large attenuations in seismic signal. White's model does this by modeling seismic waves as they pass through two concentric spheres each with different saturating fluids. Ajo-Franklin et al. (2013) combined Gassmann (1951) and White (1975) equations to estimate p-wave seismic velocity (Vp) variations with changing CO_2 saturation from a cross-well seismic tomography dataset. I apply White's model to simulate Vp changes that occur from brine being replaced with gas within the Navajo Sandstone. I use the modeled changes in Vp to calculate seismic travel time changes expected within the Navajo reservoir. I also use the modeled change in Vp to model changes in reflectivity using Zoeppritz equations (Zoeppritz, 1919).

White's model requires estimates of viscosity, bulk modulus, and density (ρ) of the fluid filled pore space; and dry rock modulus, shear modulus, absolute permeability, and porosity (ϕ) of the rock matrix. To find dry rock modulus using Gassmann's equations, I first find brine ρ and Vp within the Navajo sandstone.

Water density (ρ_w) varies with temperature and pressure and I estimate for Navajo reservoir depths.

, I calculate ρ_w from Kumar (2006) using

$$\rho_w = 1 + 1 * 10^{-6}(-80T - 3.3T^2 + 0.00175T^3 + 489P - 2TP + 0.016T^2P - 1.3 * 10^{-5}T^3P - 0.333P^2 - 0.002TP^2), \quad (1)$$

where T is the temperature in Celsius and P is the pressure in megapascals. I estimate Navajo sandstone T=16.9°C from local geothermal gradients (Heath et al., 2009, Utah Geological Survey 2012). I estimate P from

$$P = \rho_a d, \quad (2)$$

where ρ_a is the averaged density of all overlying units and d is the Navajo sandstone depth. For example, for a 250 m deep Navajo Sandstone, I estimate P=4.3Mpa.

To calculate brine density (ρ_b), I use

$$\rho_b = \rho_w + S\{0.668 + 0.44S + 1 * 10^{-6}\,[300P - 2400PS + T(80 + 3T - 3300S - 13P + 47PS)]\}, \quad (3)$$

where S is sodium chloride (NaCl) concentration and T is temperature in Celsius. I use NaCl estimates of 7615 ppm from Kampman et al. (2014). To estimate Vp of the Navajo sandstone, I estimate a bulk Vp from a nearby borehole sonic log (Figure 4.1). I use a 20% porosity estimate for the Navajo sandstone ϕ from Jung et al. (2015).

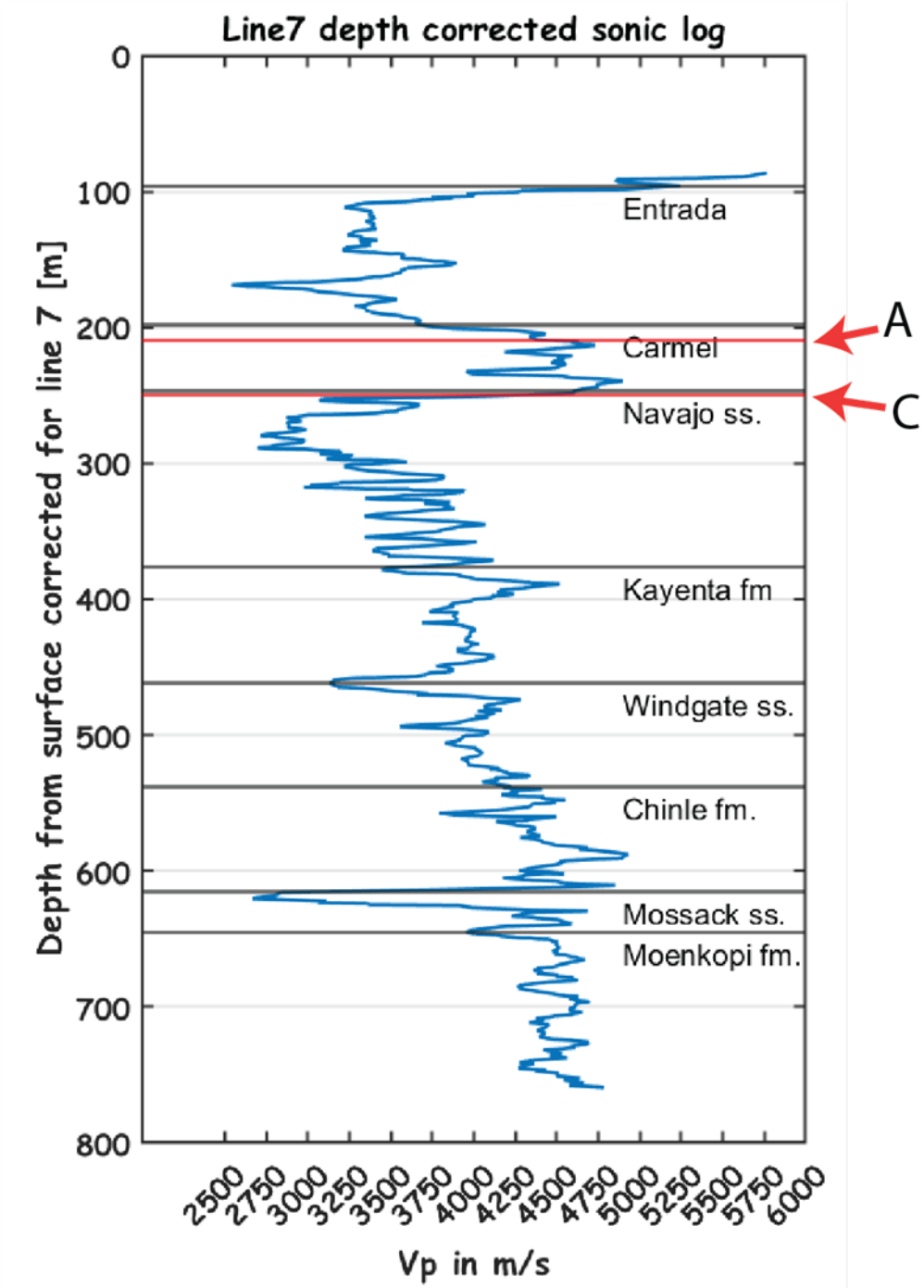

Figure 4.1 Sonic log derived from a borehole (API: 4301511138) 3km to the northwest of Crystal Geyser. Black lines are estimated unit depths for the Footwall side of the fault on Line 7. Red lines are the inferred depths of the reflectors seen in Figure 5.1.

I rearrange Gassmann's equations from Smith et. al. (2003) that require Vp, Vs, ϕ, matrix bulk modulus (K_m), brine bulk modulus (K_B), fluid density (p_b), and rock density (ρ_r) to calculate the dry rock bulk (K_{dry}) and shear modulus. The equations are as follows

$$\rho_{blk} = \rho_r(1-\phi) + \phi p_b, \quad (4)$$

$$\mu = \rho_{blk} {V_s}^2, \quad (5)$$

$$K_{s=}\rho_{blk} {V_p}^2 - \frac{4}{3}\mu * 10^{-9}, \quad (6)$$

$$K_{dry} = \frac{K_m K_s - {K_m}^2 K_B + K_m \phi K_s K_B - {K_m}^2 \phi K_s}{{K_m}^2 \phi + K_m \phi K_B - K_s K_B + K_m K_B}, \quad (7)$$

where K_m is the bulk modulus of the matrix, $K_s$is the bulk modulus of the saturated rock, K_B is the bulk modulus of the brine, ϕ is the porosity , ρ_r is the density of the rock, p_b is the density of the brine, ρ_{blk} is the density of the rock with brine filling the pores, μ is the shear modulus, K_{dry} is the dry frame modulus. I use ρ estimates for the Navajo sandstone from Naruk et al. (2019) and Stockton & Balch (1978).

To estimate the bulk modulus of brine in the Navajo sandstone, I first calculate water Vp (Vp_w)with the equation from Lubbers and Graff (1998)

$$Vp_w = 1404.3 + 4.7T - 0.04T^2. \quad (8)$$

Second, I calculate brine Vp using the Batzle and Wang (1992) equation

$$V_b = Vp_w + S(1170 - 9.6T + 0.55T^2 = 8.5 * 10^{-5}T^3 + 2.6P$$
$$= 0.0029TP - 0.0476P^2) + S^{1.5}(780 - 10P + 0.16P^2) - 820S^2. \quad (7)$$

Lastly, I calculate the bulk modulus of the brine using the following equation from Kumar (2006).

$$K_B = \rho_b {V_b}^2 * 10^{-6}, \quad (9)$$

where K_B is the brine bulk modulus.

I calculate the bulk modulus and density of the CO_2 gas within the Navajo sandstone by using a Matlab script from the RPH toolbox based on Z. Wangs measurements (Mavko et al., 2009). I use viscosity values for water and CO_2 gas taken from empirical relationships based on temperature (Engineering Toolbox, Lemmon et al., 2005). I use permeability values from Jung et al. (2015) for the Navajo sandstone and I use mineral bulk and shear modulus for quartz from the Lee (2003). I use the same value for the radius of the sphere as Ajo-Franklin et al. (2013) with a frequency of 50Hz. I calibrate my measurements by duplicating the results of Ajo-Franklin et al. (2013). All rock property calculations and measurements are summarized in Table 4.1 through Table 4.3.

Table 4.1 Fluid properties and other Whites model parameters.

Unit name	Symbol	Navajo	Carmel	Source
Density [g/cc]	ρ_r	2.4	2.6	Stockton and Balch (1978)
Vp [m/s]	V_p	3600	3850	Sonic Log (Figure 4.1)
Vp/Vs	N/A	1.8	1.8	Calculated
Porosity [0-1]	ϕ	0.2	N/A	N/A
Permeability [m^2]	N/A	5.28E-13	N/A	Jung et al., (2015)
Permeability [mD]	N/A	535.00	N/A	Jung et al., (2015)
Permeability [mD]	N/A	5349.96	N/A	Jung et al., (2015)

Table 4.2 Mineral Properties for the Navajo reservoir

Parameter	Value	Source
Mineral Bulk Modulus [Gpa]	36.4	Lee (2003)
Mineral Shear Modulus [Gpa]	44	Lee (2003)
Mineral Density [g/cc]	2.65	Lee (2003)

Table 4.3 Fluid properties and other White model parameters.

	Symbol	Value	Source
(Brine) Bulk modulus [GPa]	K_B	2.2933	Calculated
(Brine) Density [g/cc]	p_b	1.005	Calculated
(Brine) Viscosity [Pa-s]	N/A	0.0010791	Engineering Toolbox
(Gas) Bulk modulus [GPa]	N/A	0.0175	Batzle and Wang (1992)
(Gas) Density [g/cc]	N/A	0.1986	Batzle and Wang (1992)
(Gas) Viscosity [Pa-s]	N/A	1.47E-05	Lemmon et al., 2005
(Gas) Saturation range	N/A	0-1	N/A
Radius of sphere [cm]	N/A	1	Ajo-Franklin et al. (2013)
Frequency range [Hz]	N/A	50	Ajo-Franklin et al. (2013)
Temperature at depth [Celsius]	T	16.9	Heath et. al., (2009)

Zoeppritz Equations

I use the E.S. Kerebes (1991) approach that uses Zoeppritz equations to calculate the reflection coefficient at a given incidence angle (Zoeppritz, 1919) from the top of Navajo Sandstone. I calculate the incidence angle using a 250 m deep Navajo Sandstone (Kampman et al., 2014), the range of seismic source and receiver offsets used in my field test, and the velocities shown in Table 4.1. This approach requires Vp, Vs and rock ρ for both the Carmel and Navajo formations. I use the Vp output for the from White's model and ρ from Stockton and Balch (1978) for the Navajo sandstone. I use ρ, Vp and Vs estimates for the overlying Carmel formation from Stockton and Balch (1978) where the base of Carmel formation is reported as the Dewy Bridge member. I calculate Vs for both units using the following empirical equation for clastic sedimentary rocks from Castagna et al. (1985).

$$V_s = (V_p - 1.36/1.16). \quad (11)$$

Using these inputs, I calculate the reflection coefficient at all measured distances for the full range of CO_2 gas saturation. These results are shown in Chapter 6.

CHAPTER FIVE: SEISMIC DATA ANALYSIS

Common Offset Phase Picking and Processing

To explore possible seismic changes resulting either from acquisition methodologies or from changing CO_2 content, I sort unprocessed field records from each 10-hour daily window into common channel, or common offset gathers (Figure 5.2). For my body wave analyses, I apply a 40 to 240 Hz bandpass filter to improve the signal quality. I use the Seismic Unix (Stockwell & Cohen, 2008) sumax routine to automatically extract maximum amplitude and its travel time with in a manually selected bounding window that contains the phase of interest. This is done for both the first arrivals and reflectors A and C based (Figure 5.1). I determine a noise threshold for each trace using root mean square values during the first 0.025 seconds of each common offset gather. This assessment allows me to identify noisy traces (e.g., mis-triggers, wind noise, etc). This exercise removed about 25% of the field data. The majority of the data removed was from seven traces adjacent the source on both sides where amplitudes for first arrivals are high and exceed my threshold. With my automated approach, there was no picking bias introduced.

I convert amplitudes for both reflections and first arrivals into a z-score and plot trace offset for each day. I computed Z-score using the following formula

$$Z = \frac{x - \mu}{\sigma}, \quad (12)$$

where x is the observed value, μ is the mean of the picked amplitude values for that trace or offset, and σ is the standard deviation of those values. This analysis is conducted across the full 10-hour window on a trace by trace basis. A high amplitude will result in a positive z-score and a low amplitude will result in a negative z score. This conversion from amplitude to z-score normalizes the data and removes amplitude variation with offset. This allows for comparison of amplitude behaviors across different parts of the array.

I convert travel time for my auto picked first arrivals into residuals by subtracting first arrival times picked from a summed shot gather that represented the travel times for the first 50 minutes for each day (Figure 5.1). I process reflection travel times into residuals by fitting a second order polynomial (equation 12) to the median value of each offset for the whole window and subtracting the value of that fit from each offset. The equation is as follows

$$m = xa^2 + xb + c, \quad (13)$$

where m is the median value of a specific offset x and a through c are fitted coefficients.

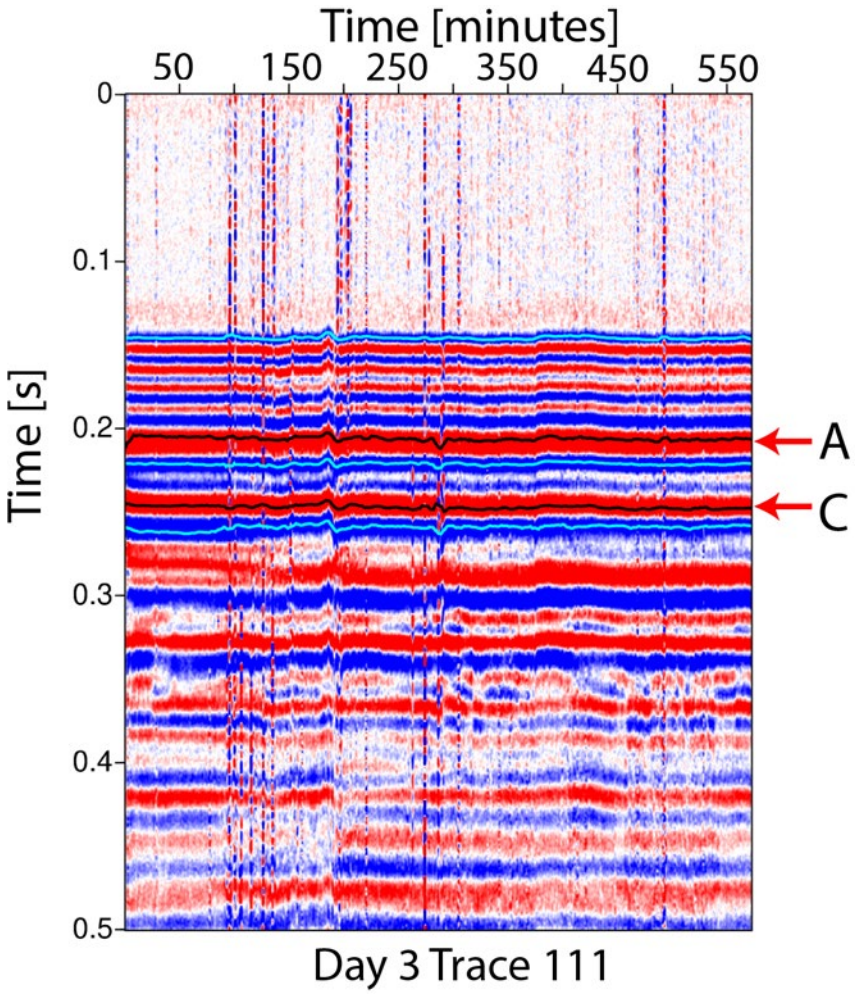

Figure 5.1 Common trace or offset gather (111) with a 40 to 240 Hz bandpass filter. Maximum and minimum amplitudes for the reflectors and first arrivals are black and cyan plotted lines. Reflector's "A" and "C" are the same as those seen in Figure 5.3.

Time-lapse Amplitude and Travel Time Assessment

For time-lapse comparisons and phase identifications from my baseline measurements, I sum the first 100 shot gathers that represent a 50-minute time window (Figure 5.1). This approach reduces random noise by the number (n) of repeated hits by $\sqrt{n}$ or about a factor of seven. I identify distinct phases on this shot gather and explore for changes during my 30-hour experiment. I focus on relative travel time and amplitude changes for three distinct phases or arrivals. I focus on first arrivals that represent Vp

diving waves that probe the upper 10's of meters (Yelton, 2021), surface waves that mostly represent Vs structure for the upper 10's of meters (e.g., Xia et al., 1999), and reflections that represent reservoir boundaries where CO_2 gas is trapped. I focus on shallow velocity structure because of the large and spatially varying CO_2 flux that has been documented along Line 7 (Jung et al., 2014) and because of the pronounced low Vp and Vs damage zone related to the LGWF that was recently characterized (Yelton, 2021; Figure 3.2). With my approach, I disregard absolute velocities and simply focus on travel time and amplitude changes for a 30-hour window.

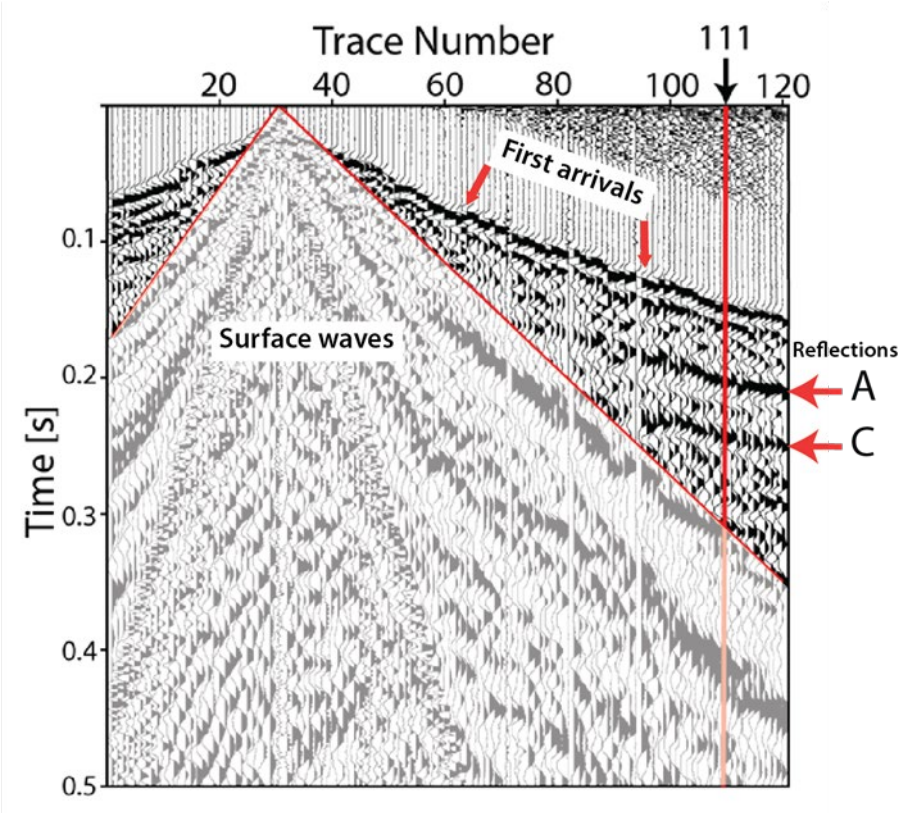

Figure 5.2 Sample shot gather that has been summed, filtered and gained showing first arrivals, surface waves, and the two primary reflectors A and C. I show the trace 111 common offset gather at 392.5 m for Day 3 in Figure 5.2. Receiver offsets range from -162.5 to 437.5 m.

Surface Wave Analysis

I analyze the seismic records for changes in surface (Rayleigh) wave speeds by summing five unprocessed shots gathers that account for an elapsed time of 2.5 minutes (30 seconds per record). This summation improves surface wave phase velocity coherence. I separately assess receiver locations located above the LGWF hanging wall using geophones 1-60 (-152.5-147.5 offset) and receiver locations located above the LGWF foot wall using geophones 80-120 (247.5-447.5m offset). Since the seismic source lies above the hanging wall side of the LGWF, the lower numbered receivers record surface wave speeds within the Mancos Shale unit that lies entirely within the hanging wall block (Figure 3.2). In contrast, the higher numbered receivers record surface wave speeds that are influenced by shallow hanging wall, shallow footwall and LGWF damage zone strata.

I examine the Rayleigh wave dispersion curves using the approach of Xia et al. (1999). I focus only on the fundamental (lowest phase velocity) mode, and I remove body wave energy by muting signals that arrive before the surface waves. I generate dispersion curves for each gather, and I explore for changes in phase velocities for the full 30-hour time-lapse window. Given that the phase velocities range from 500 to 1000 m/s for frequencies that ranged from 10 to 30 Hz, I explore wavelengths that range from 50 to ~330 m.

CHAPTER SIX: RESULTS

Overview

In this chapter, I first present my Crystal Geyser eruption catalog and how eruptions change through time. I then show the results of seismic velocity and amplitude modeling and how they inform my expectations of the seismic data. Lastly, I present the time-lapse data for first arrivals, reflections, and surfaces waves and my interpretations of that data.

Navajo-sourced Geyser Eruptions Derived from Temperature Data

Kampman et al. (2014) noted that the Crystal Geyser B- and D-type eruptions have a bimodal eruption pattern that shows eruption duration increasing over the past decade and a half. In this section, I aim to characterize the eruption patterns of the Crystal Geyser observed with my data set and compare my results to previous studies to identify changes in eruption behavior over multiple years.

To extract eruption characteristics, I compare temperature measurements from three sources. I compare air temperature data from the MOAB Canyon Field Station, located about 60 km to the southeast from Crystal Geyser (Figure 6.1) with my transducer temperature data that record either air or water temperature at Crystal Geyser. I also utilize water temperature data from a Green River gage station, located 5.5 km to the north of the Crystal Geyser. Although the gage station did not record water temperature in November 2020, I utilize measurements from the same time window in 2021.

I note a difference in the air and geyser sensor temperatures that are consistent with eruption patterns identified by Han et al. (2013) and Kampman et al. (2014) (Figure 6.2). Given the cold nighttime air temperatures during our November and December field campaign with respect to the warm water geyser eruptions, I was able to identify and characterize repeated eruptions for the 30-day recording window (Figure 6.3). I confirm these eruptions with both visual camera data and constant 16.9°C geyser temperatures. I identify near-daily footwall-based Navajo sandstone-based eruptions (see Figure 2.2), and I divide these into class type as defined by Kampman et al. (2014) and references within. I classify the 0.5 to 1.0 hour duration eruptions as B-type. These eruptions have a six to ten hour recharge interval. The D-type eruptions last 20 to 27 hours and have a recharge interval of 65-75 hour. A and C type eruptions are small "bubbling events" that occur between B and D type events. River temperatures in 2021 steadily decreased from 10°C to about 2°C over the same 30-day window, suggesting that the river temperature is driven by air temperature and that the geyser water temperature was not directly influenced by river water temperature.

I observe some daytime (7am-7pm) geyser temperature peaks that rise above 16.9°C (Figure 6.2). Although Han et al. (2013) and Kampman et al. (2014) identified higher temperature eruptions that presumably were sourced from deeper reservoirs, I speculate that many of my anomalously high temperatures resulted from sunlight warming (radiative forcing) within the borehole-coupled sensor. This is supported by the presence of these higher temperature readings only during daylight hours and that my camera captured no eruption on November 11th when transducer temperatures approached 20°C (Figure 6.2). Similarly, I note some lower temperature differences

between air and geyser temperatures during nighttime hours that may reflect A and C type eruptions. But, because I could not fully characterize these events from my single temperature sensor, I only focus on B- and D type Navajo-sourced eruptions which show a constant and repeatable temperature from outflow at the Crystal Geyser. Additionally, the recharge interval will be defined as the time between B-and D-type eruptions.

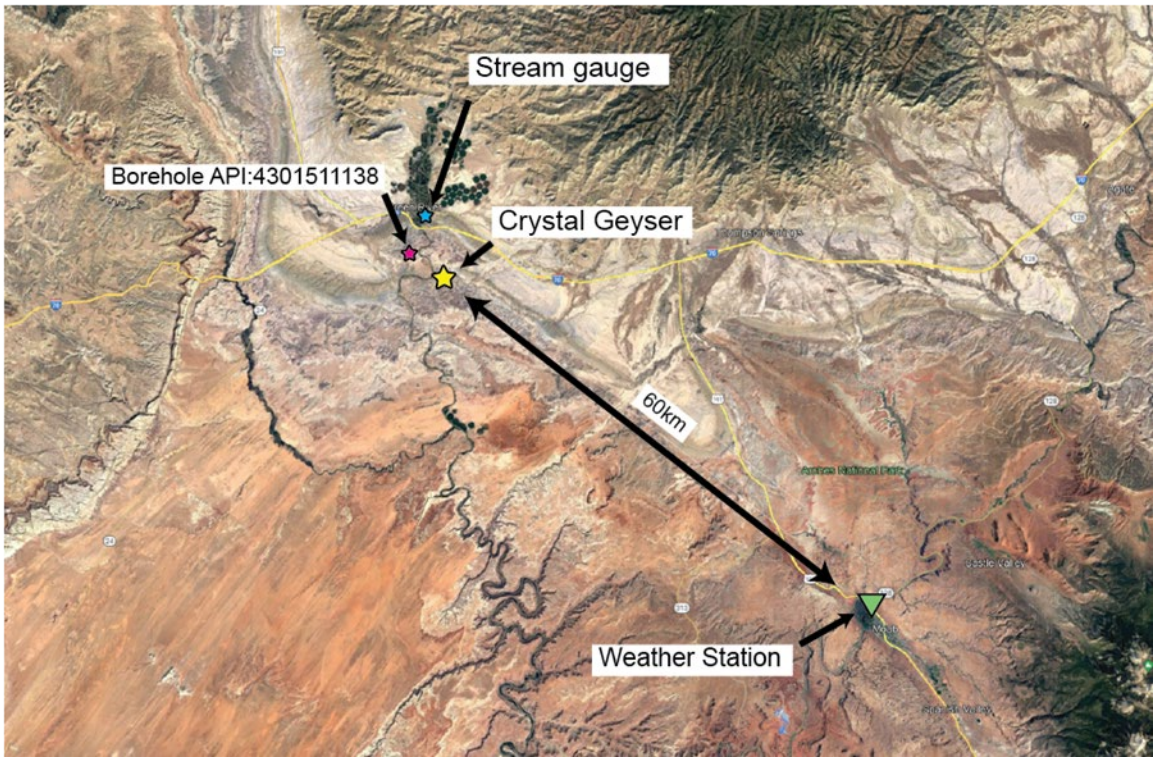

Figure 6.1 Map of greater Crystal Geyser area. Green triangle is the location of the MOAB Canyon Field Station relative to the Crystal Geyser (yellow star). Borehole that contains the sonic log seen in Figure 4.1.

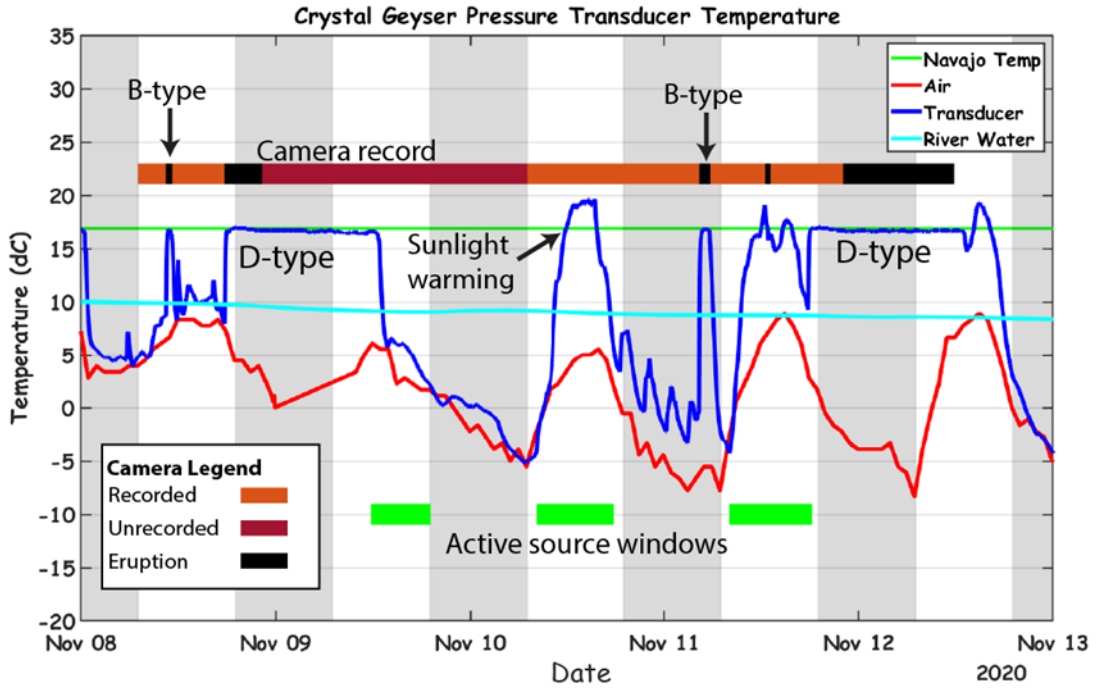

Figure 6.2 Field campaign window from Nov 8th to 13th with overnight hours (7pm-7am) shaded in grey. Black and green rectangles are camera recorded eruptions and time-lapse seismic recording windows. Camera captured windows are in orange and unrecorded windows are in red. I interpret D-type eruptions overnight on Nov 9th and 12th and B-type eruptions mid-day on Nov 8th and early morning on the 11th.

Air temperatures at the Moab field station ranged from -17 to 22°C, with an average air temperature of 2.8°C (Figure 6.4). Daily temperature fluctuations ranged from 8 to 30°C. Green River water temperatures show two peaks during 2021 and generally suggest that air temperature controls the river water temperature. The river water show little variation between daytime and nighttime hours. Crystal Geyser temperatures show mostly higher temperatures when compared to air temperatures, but with a similar distribution for about 73% of the time. However, the geyser remained at or near 16.9°C for about 27% of the total 30-day window. This constant temperature reflects reservoir

temperatures from the footwall block of the Navajo Sandstone (Kampman et al., 2014; Probst et al., 2018) (Figure 2.2) and suggests regular geyser eruptions.

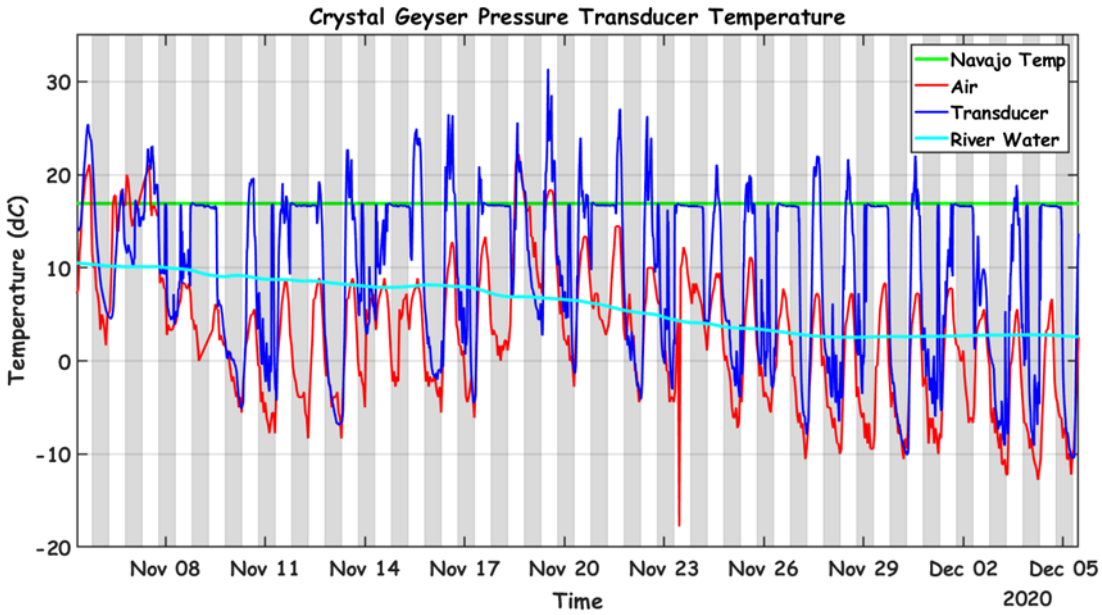

Figure 6.3 30-day Temperature record from November 5th – December 5th 2020 with overnight hour (7pm-7am) shaded in gray. Well head transducer shown in dark blue, air temperature from MOAB weather station shown in red and the Green River water temperature shown in light blue.

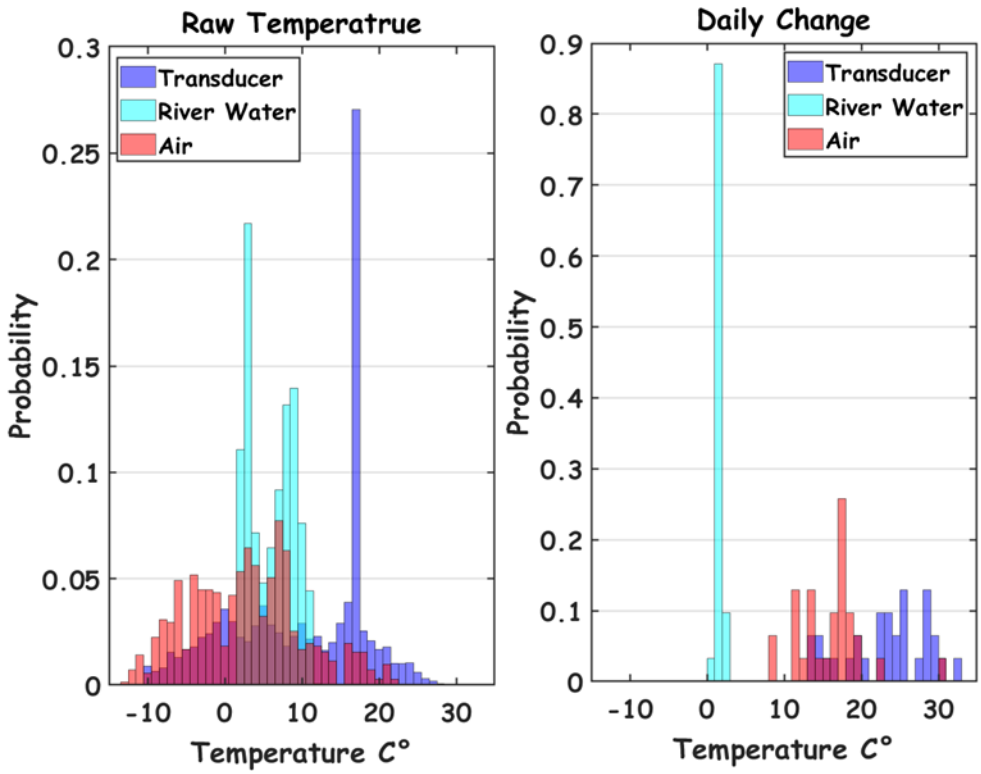

Figure 6.4 Probability mass function histograms showing temperature distributions of river water (light blue), transducer (dark blue) and air (red) over the 30-day recording window. Left figure shows raw continuous data. Right figure shows daily temperature change which is the difference between daily minimum and maximin values.

I identify 10 D-type long-duration events and 14 B-type short-duration events presumably sourced from the Navajo sandstone during my 30-day recording (Figure 6.3). My eruption classification results are consistent with Kampman et al. (2014) B- and D-type eruption events (Figure 6.5). However, my recorded D-type events have a shorter recharge interval (32-47 hours) and duration (15-21) when compared to Kampman et al. (2014) (65-75 hour interval and 20-27 hour duration). In addition, Han et al. (2013) found that D-type eruptions had a very different duration and eruption interval in 2008 with eruptions only lasting 5 to 7 hours and with an 18–28-hour delay between cycles. When I calculate the percentage of the cycle time that the geyser is experiencing a D-type eruption, I observe that active D-type eruptions comprise about 35% of the cycle time.

When I compare this to previous studies, I note a consistent increase over time starting from 9% in 2006 (Figure 6.6). This suggests that the geyser had erupted more often over the past few decades.

In summary, long-duration eruptions are consistently sourced from the Navajo Sandstone reservoir, and the ratio of eruption periods to dormant periods has increased with time. Coupled with a decrease in average eruption heights through time, Han et al. (2013) speculated that the Crystal Geyser may be slowly losing CO_2 and recharge rates may be diminishing. However, it may be that total discharge volume has remained constant with time, but with reduced upward mobility. This scenario may be caused by material slowing filling the borehole which was noted by previous researchers (Han et al., 2013). Another possibility is the precipitation and dissolution of material in the well bore causing flow paths of the geyser system to change (Han et al., 2013).

Table 6.1 Summary of Crystal Geyser eruptions from this study, Han et al. (2013) and Kampman et al. (2014).

Source	Eruption Type	Number recorded	Duration (hour)	Time until next eruption (hour)
This Study	D-Type	10	15-21	32-75
This Study	B-Type	14	1-2	5-15
Kampman et al., (2014)	D-Type	5	20-27	60-75
Kampman et al., (2014)	B-Type	N/A	N/A	N/A
Han et al., (2013)	D-Type	6	5-7	15-27
Han et al., (2013)	B-Type	7	1-2	5-10

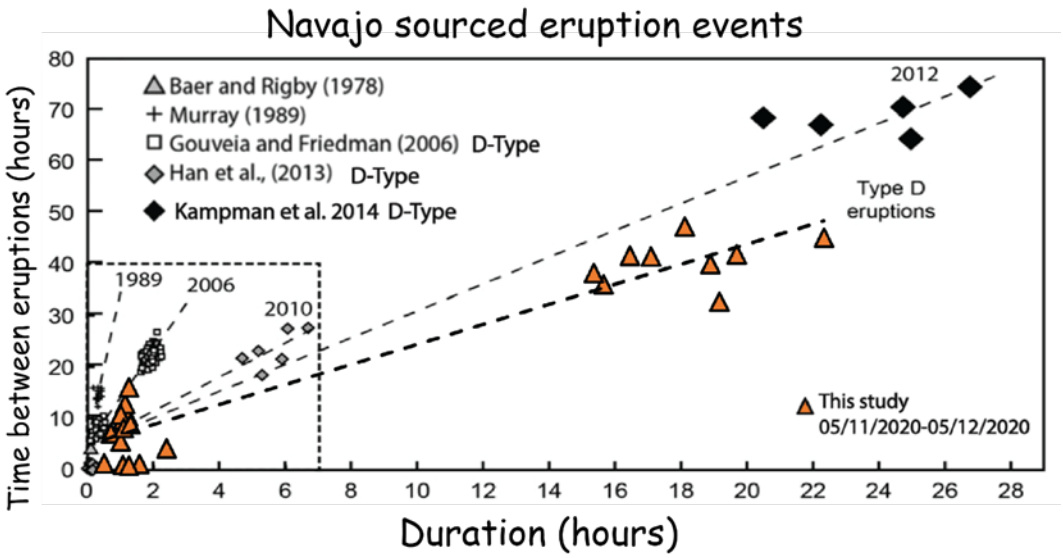

Figure 6.5 Modified from Kampman et al. (2014), showing Navajo sandstone-derived geyser eruptions from past studies and during our November 2020 campaign.

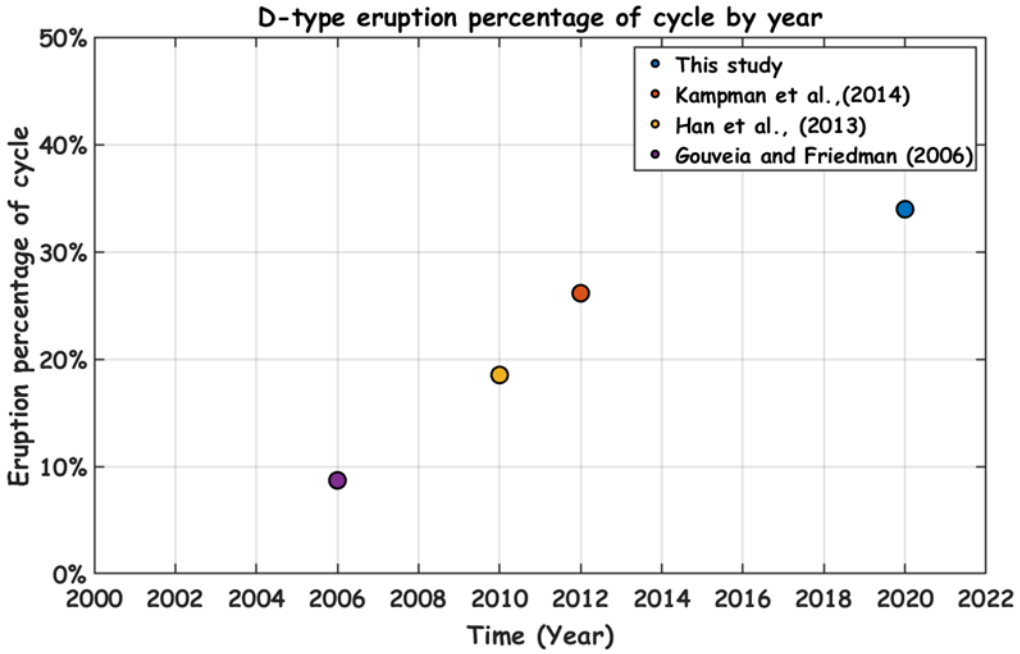

Figure 6.6 Plot showing how D-type eruption as a percentage of eruption cycle has changed over the last 15 years.

Patchy White Modeling

To explore seismic velocity changes in the presence of gas within the Navajo Sandstone, I use the Patchy White model (White, 1975). My Patchy model results shows that the greatest gas-driven reduction in Vp lies near a 12% gas saturation (Figure 6.7). For example, I model Vp= 3600m/s for full fluid saturated Navajo sandstone. Vp rapidly decreases to a minimum Vp of 3410m/s, or a 5.2% reduction, in the presence of 12% gas saturation. At higher saturations, Vp decreases from the full fluid state, but increases above the Vp for 12% gas saturation. This is consistent with trends noted by Ajo-Franklin et al. (2013).

Given a 100 m thick fluid saturated Navajo Sandstone layer, two-way travel time through the reservoir measures about 55.5 milliseconds (ms). This same travel time path for 12% CO_2 saturated Navajo Sandstone reflector increases to about 58.6 ms or about a 3 ms travel time lag. This travel time change is near my measurement threshold (three samples at one millisecond sample rate). Given that the Navajo Sandstone is likely always partially CO_2 saturated, the travel time residual would likely be much less than 3 ms for my survey. I speculate that it would be difficult to confidently capture travel time changes through the Navajo Sandstone reservoir using surface-based seismic measurements as this reservoir is already partially saturated with CO_2.

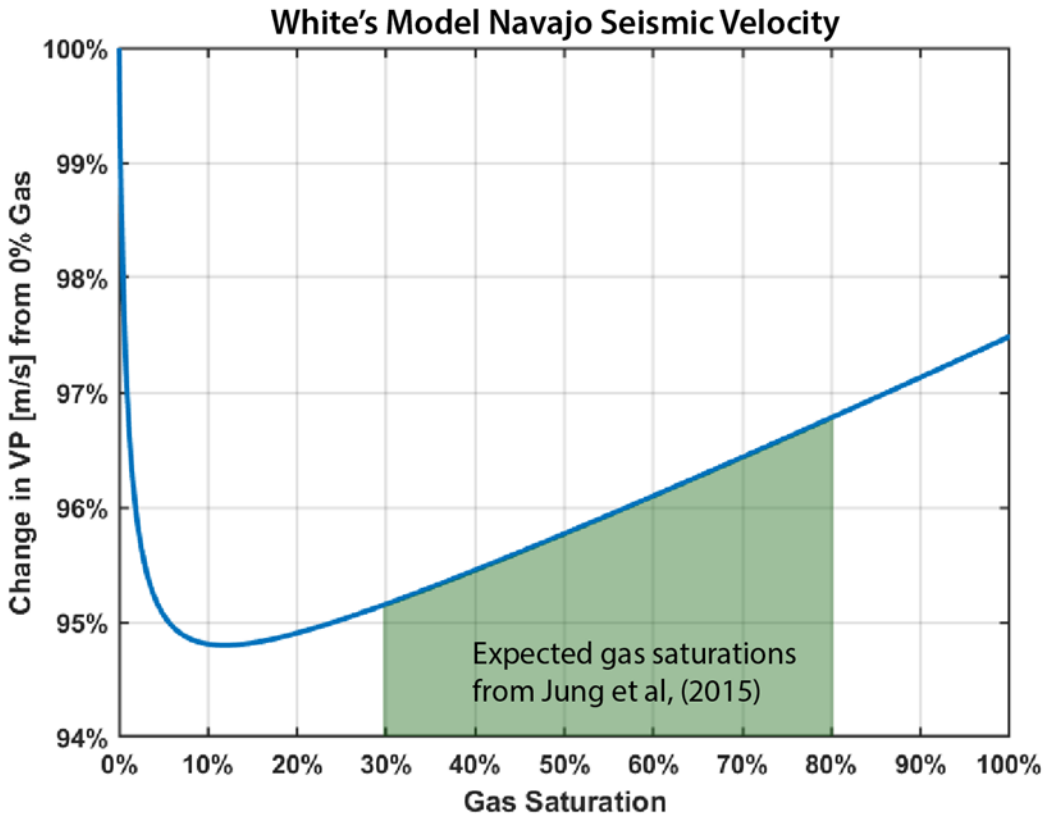

Figure 6.7 Graph showing change in Vp within the Navajo sandstone from my Patchy model. Here, I use a baseline of 3600 m/s that represents Navajo Sandstone.

Zoeppritz Modeling

Zoeppritz models add the offset or angle dependence of seismic amplitude. For this model, I explore the reflection coefficient, or anticipated change in reflection amplitude along reflector "C" in the presence of changing gas conditions within the lower unit (Figure 5.1 and Figure 5.2). I interpret this reflector's amplitude to represent the Vp contrast observed when transitioning from the Carmel to Navajo units. This interpretation is based on reflection arrival times calculated using stacking velocities and depth to the Carmel/Navajo boundary (Figure 4.2). In the presence of no gas, I expect a negative impedance along "C", as the Navajo Sandstone Vp is less than the Carmel Formation Vp. With increasing Navajo gas content, the impedance contrast would increase, or become

more negative (Figure 6.8). In the presence of no gas, my model shows the reflection coefficient can vary with offset by upwards of 20%. This variation is simply related to the angle dependence of seismic amplitude with offset. When modeling the full range of gas saturation for the Navajo unit, I show that the greatest changes in reflection coefficients will occur at gas content between 0 and 12% for all offsets. I observe that the reflected amplitude can change by upwards of 50%, depending on offset (or angle). This analysis reinforces that amplitude changes with offset are more sensitive to changing reservoir properties at low CO_2 saturations at all reflection angles.

I note a few caveats to this analysis and assessment. First, given the partially saturated conditions that likely persist along the LWGF, I speculate that amplitude changes are near my measurement threshold with my seismic approach. Second, this analysis assumes that the Carmel Formation contains no gas or that gas does not migrate upward across this high impedance boundary. Third, I assume that this reflector represents the large impedance contrast at the Carmel/Navajo contact. Because there is no direct borehole control along Line 7, I cannot be sure that I have modeled the proper Vp impedance contrast. For all of these reasons, my z-score reflection analysis presented below simply explores relative amplitude changes across a high impedance boundary with unknown levels of gas saturation.

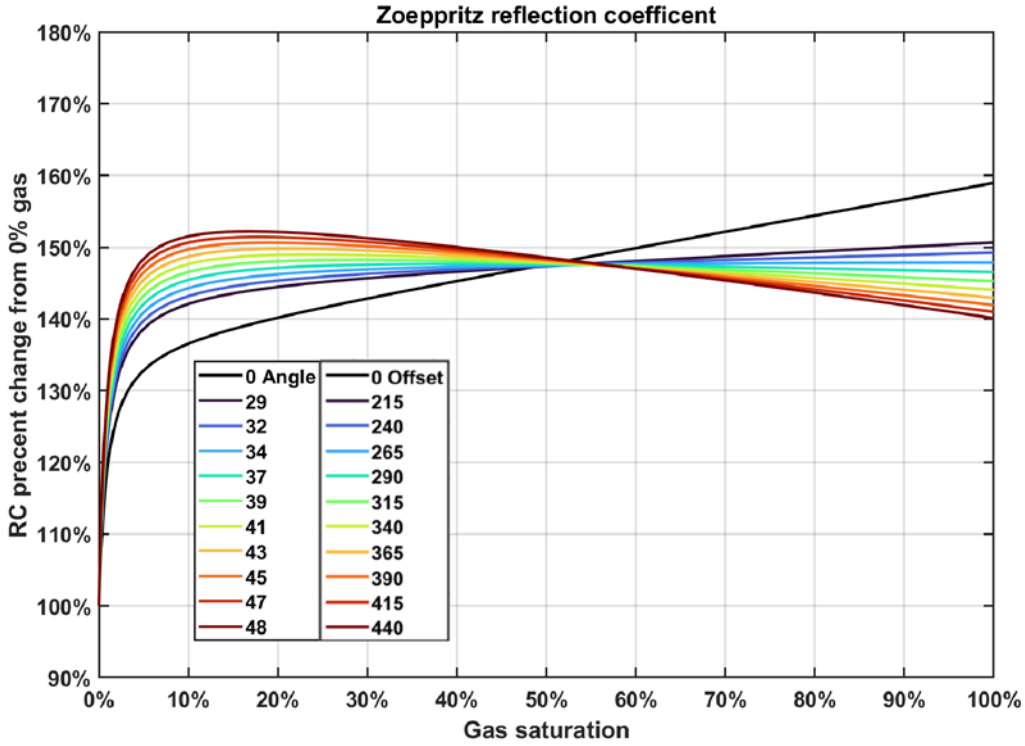

Figure 6.8 Graph showing percent change in the reflection coefficient with changing gas percentage as a function of offset (meters) and reflection angle.

First Arrival and Reflection Z-score and Travel Time Residuals

Modeling from the previous section shows that gas saturation can cause observable changes in seismic travel times and amplitudes. I hypothesize that I may be able to identify changes in the first arrivals or reflections that relate to changing gas saturations at or above the Navajo reservoir. If positively correlated with eruption cycles at the Crystal Geyser, it would show connectivity between the geyser and reservoir properties located one km to the east. I can also assess the repeatability of the seismic survey with this analysis.

I relate the two identified reflections “A” and “C” to Entrada/Carmel and Carmel/Navajo lithologic boundaries respectively (Figure 4.1). Unfortunately, I did not confidently identify a reflector from the base of the Navajo unit that would best show

travel time residuals from the primary reservoir. I measure reflection amplitude and arrival times for the two identified reflectors and generate z-scores and residuals for three acquisition days. I explore changing signals and compare both first arrival and reflection data with Crystal Geyser eruption cycles identified from temperature data.

As sources of changing noise or signal, I consider 1) cultural signals that include car or train signals; 2) wind noise; 3) seismic source effects, 4) human foot traffic and 5) CO_2 gas movement. Car traffic would emanate along the only road through the survey line as it is the primary access road to Crystal Geyser (Figure 3.2). Car noise typically has a frequency of 5 to 30 Hz, but would be transient and only last for a few minutes. Thus, I expect that these signals would appear on only a few adjacent shot records at most which would not cause a significant change in the z-score trend. Unique characteristics of train noise include coherent one to 20 Hz signals (e.g Pinzon-Rincon et al., 2021) that emanates from the north and pass through the town of Green River (approx. 5 km to the north) (Figure 6.1). These signals have a duration upwards of one hour. The train schedules were not available, but train passage was restricted to no more than twice daily. Wind noise has a higher z-score with broad band spectral content that ranges from about 1-100 Hz. These signals can last from minutes to hours, are generally quieter at night, and can be clearly seen in the common offset gathers of Figure 6.9 within the window before the first arrivals.

Figures 6.9 through 6.11 show that the accelerated weight drop source was very repeatable. Although our seismic source was repeatable, source characteristics were influenced by the tilting of the source hammer plate due to ground deformation from repeated soundings as well as the compaction of the ground itself. When the plate was

noticeably tilted from repeated ground hits, we re-leveled the plate during acquisition. This plate reset is best observed in the common offset gather of Day 2 (Figure 6.10) where travel time disruptions appear as sharp jogs in seismic arrivals. Human foot traffic along the seismic line is characterized by a short-duration (on the scale of minutes) anomalously high z-score that slowly travels down the array through time.

Assuming gradual changes in CO_2 gas movement, as observed at the Crystal Geyser, I expect amplitude and travel time changes to appear over a scale of hours within the fault zone. First arrivals will slow and attenuate in the presence of gas, resulting in a z-score decrease and travel time increase. An increase or decrease in reflection amplitude may be observed, depending on if reservoir gas saturation is increasing or decreasing. If the geyser is indicative of a regional outgassing CO_2 pulse, I expect to see a decrease in reflection amplitude as gas content depletes and the reverse during a recharge phase. However, no previous studies have indicated whether gas pulses along Line 7 or at any other location along the LGWF at the time scales of my survey. Where no z-score is identified (blank areas of Figures 6.12,13,15,16,17), either the original measured amplitude exceeded the RMS threshold, or the trace could not be picked.

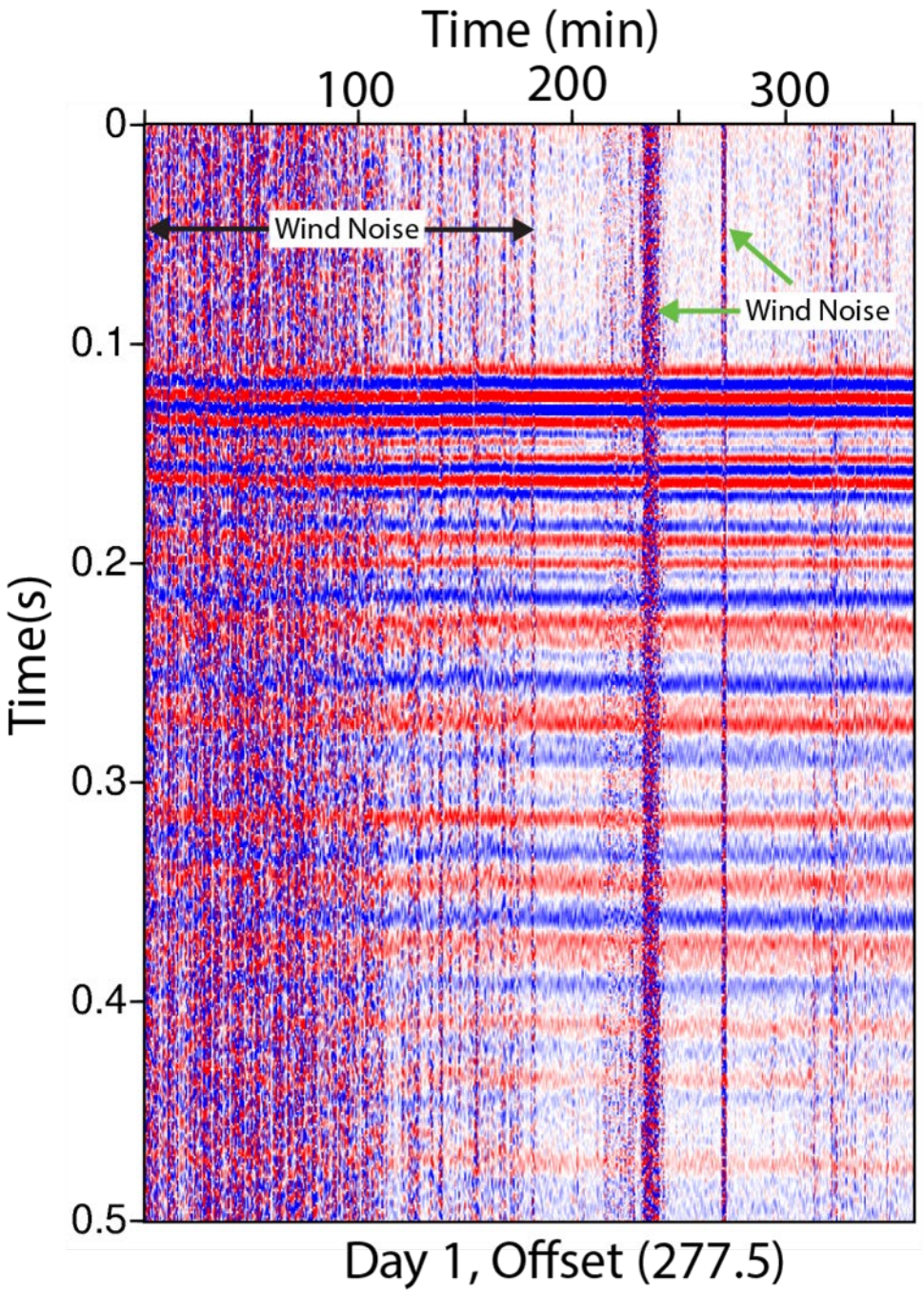

Figure 6.9 Common offset gather of trace 87 (Offset 277.5m) on Day 1 showing wind noise primarily from 0-175 minutes and another band around 240 minutes.

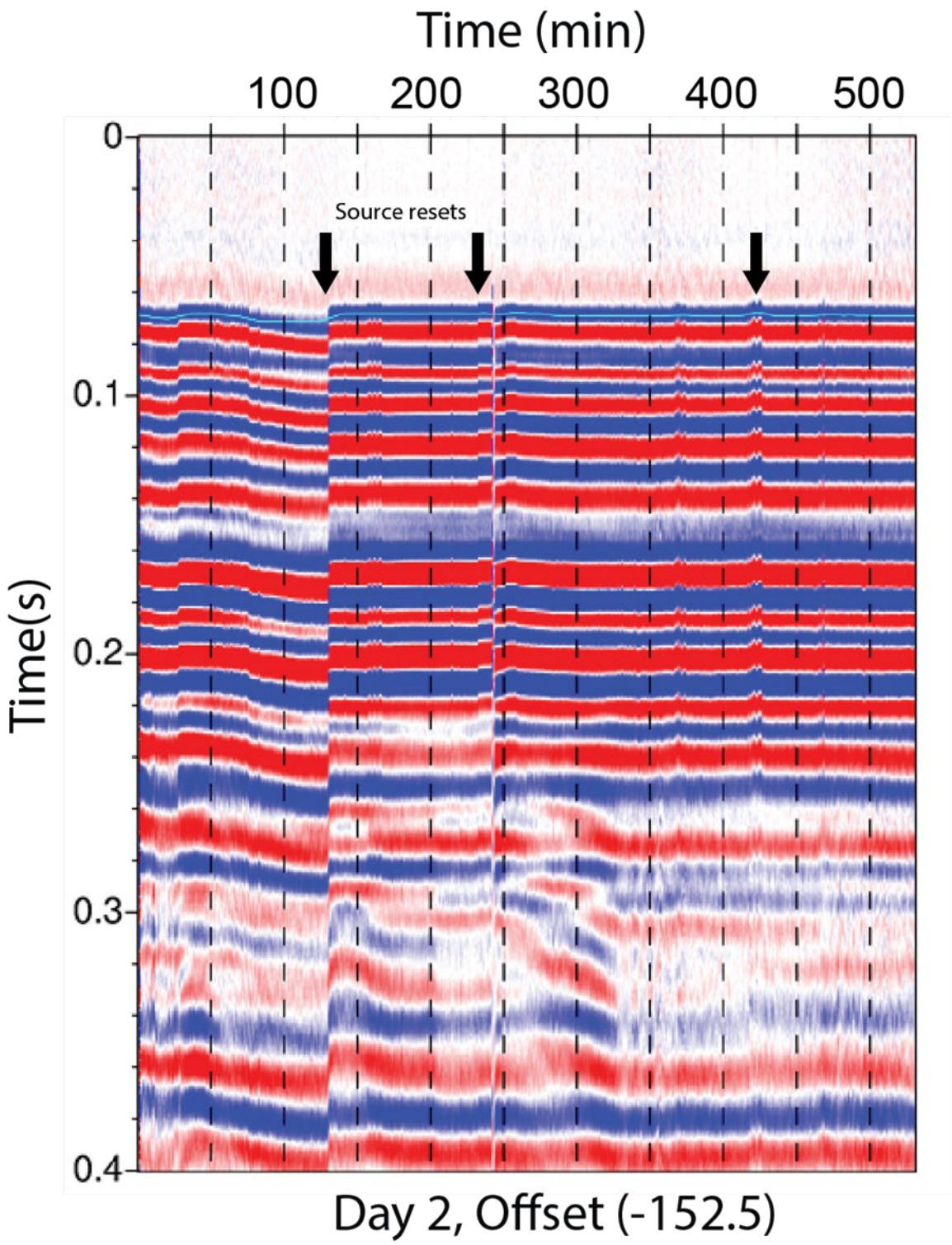

Figure 6.10: Common offset gather of channel 1 on day 2. Black arrows indicate where plate resets can be easily seen in the seismic data due to a shift in travel time. Light blue line in the first arrivals represents peak amplitude pick.

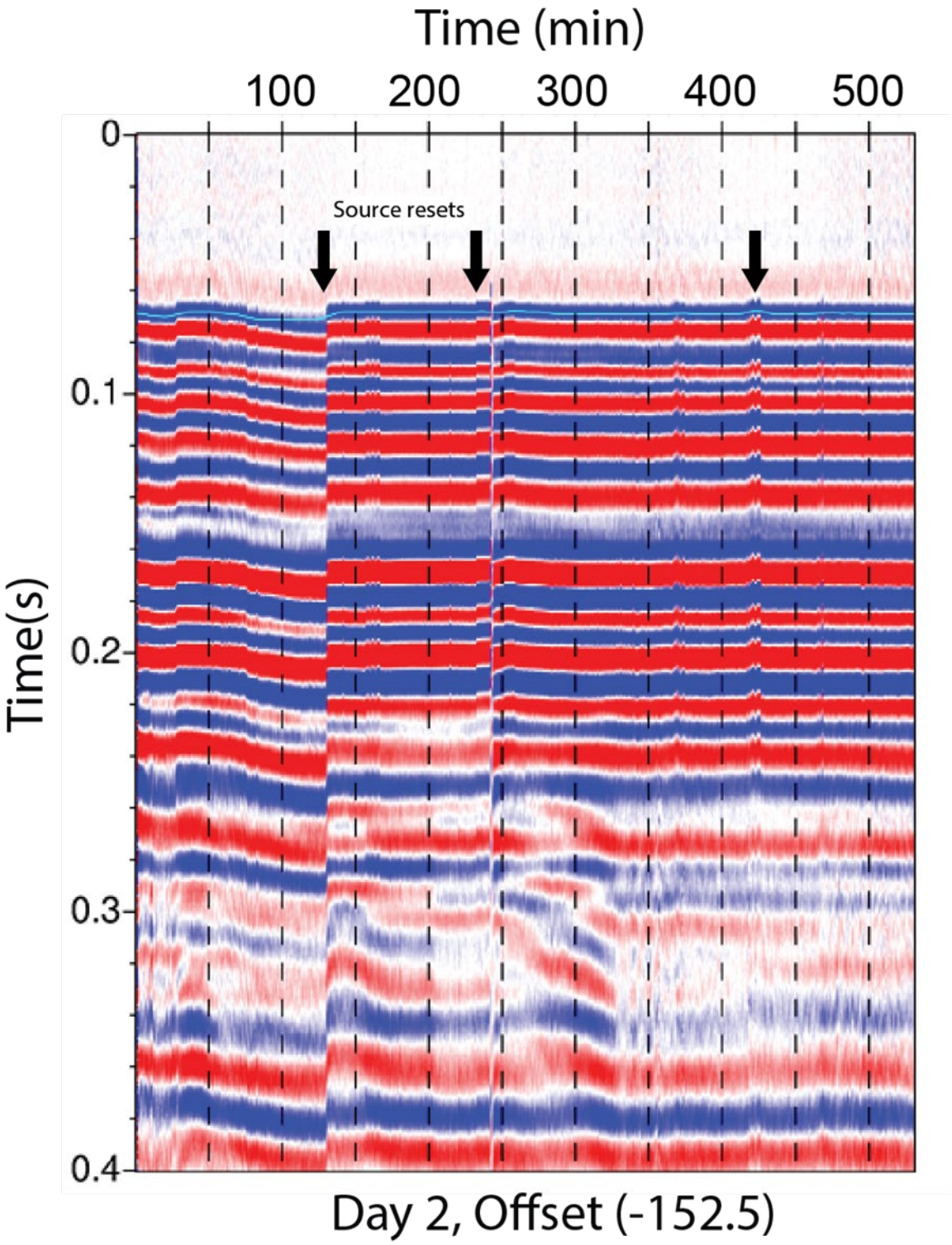

Figure 6.11 Common offset gather of channel 1 on day 2. Black arrows indicate where plate resets can be easily seen in the seismic data due to a shift in travel time. Light blue line in the first arrivals represents peak amplitude pick.

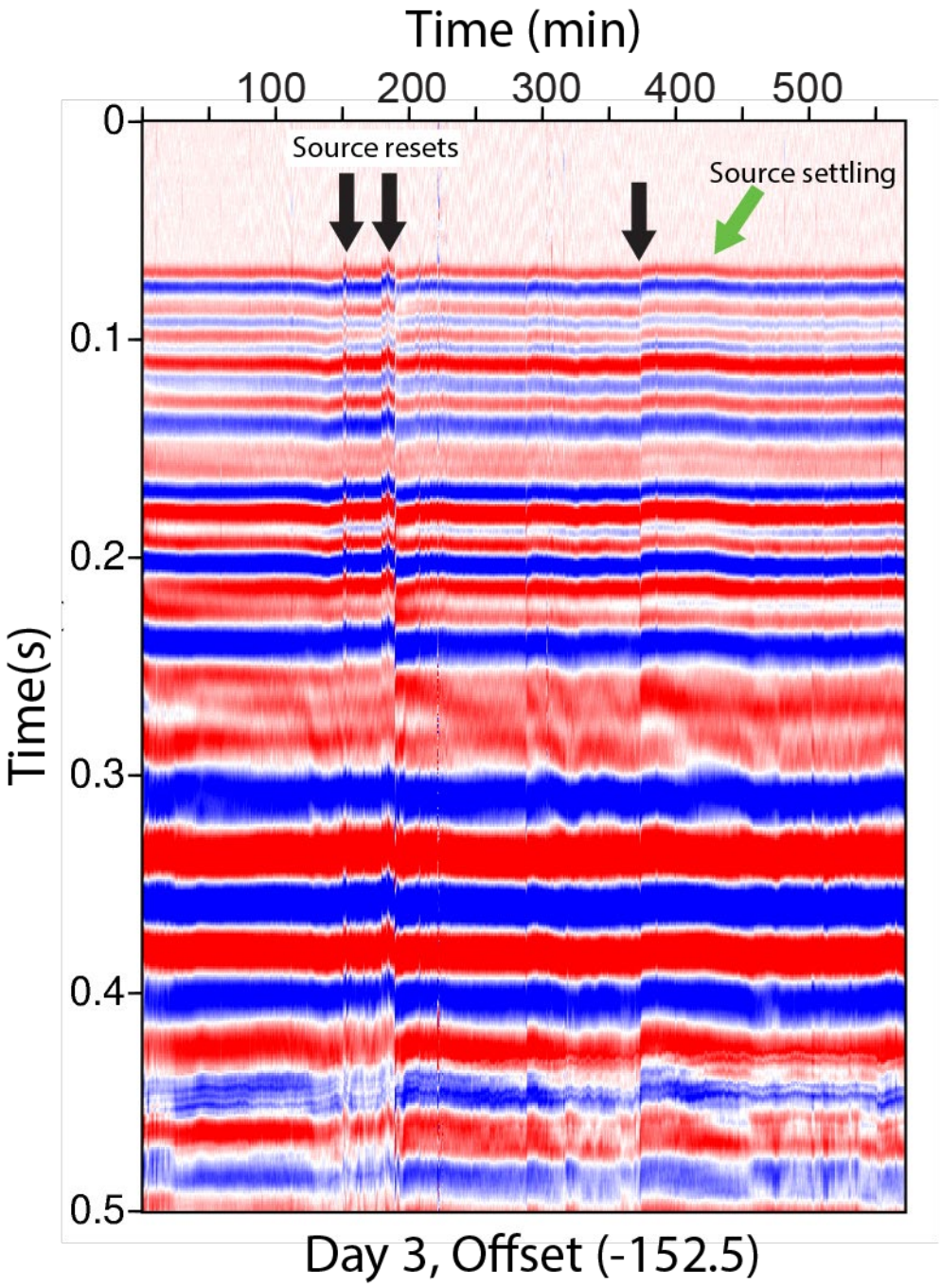

Figure 6.12 Common offset gather of channel one on day three. Black arrows indicate where plate resets can be easily seen in the seismic data due to a shift in travel time. Green arrow denotes a shift in travel time from source settling noted on field notes.

Day 1

Time lapse seismic data for Day one data includes a 120-channel 10-second vertical geophone recordings acquired every thirty seconds between 11:43:13 and 19:03:42 Mountain Standard time on November 9, 2020 (Figure 6.12). I note that the recordings initiated at the tail end of a 60-minute D-type eruption at the Crystal Geyser. The remaining time-lapse window included no geyser eruption (right panel figure 6.12). From first arrival travel times and amplitudes, I observe a high z-score across most geophone locations or offsets and during the start of the survey that persist through 225 minutes (center panel Figure 6.12). I also observe time bands of about 5-10 minutes with high z-score occur around 250 minutes primarily in the positive offsets. In the common offset gathers both signals contain a broad band frequency of up to 150 Hz. I speculate both high z-score zones to represent wind and/or cultural noise based on the frequency characteristics seen in the common offset gathers (Figure 6.9). I speculate that the far offsets show less wind noise due to their sheltered location in the canyon. Reflection data show similar z-score characteristics to the first arrivals caused by wind noise (Figures 6.16 and 6.17). I observe no evidence of changing z-score through time that I can attribute to steady amplitude or travel time changes in the first arrivals or reflectors. I note that first arrival and reflection travel times do not show any statistically relevant changes through time.

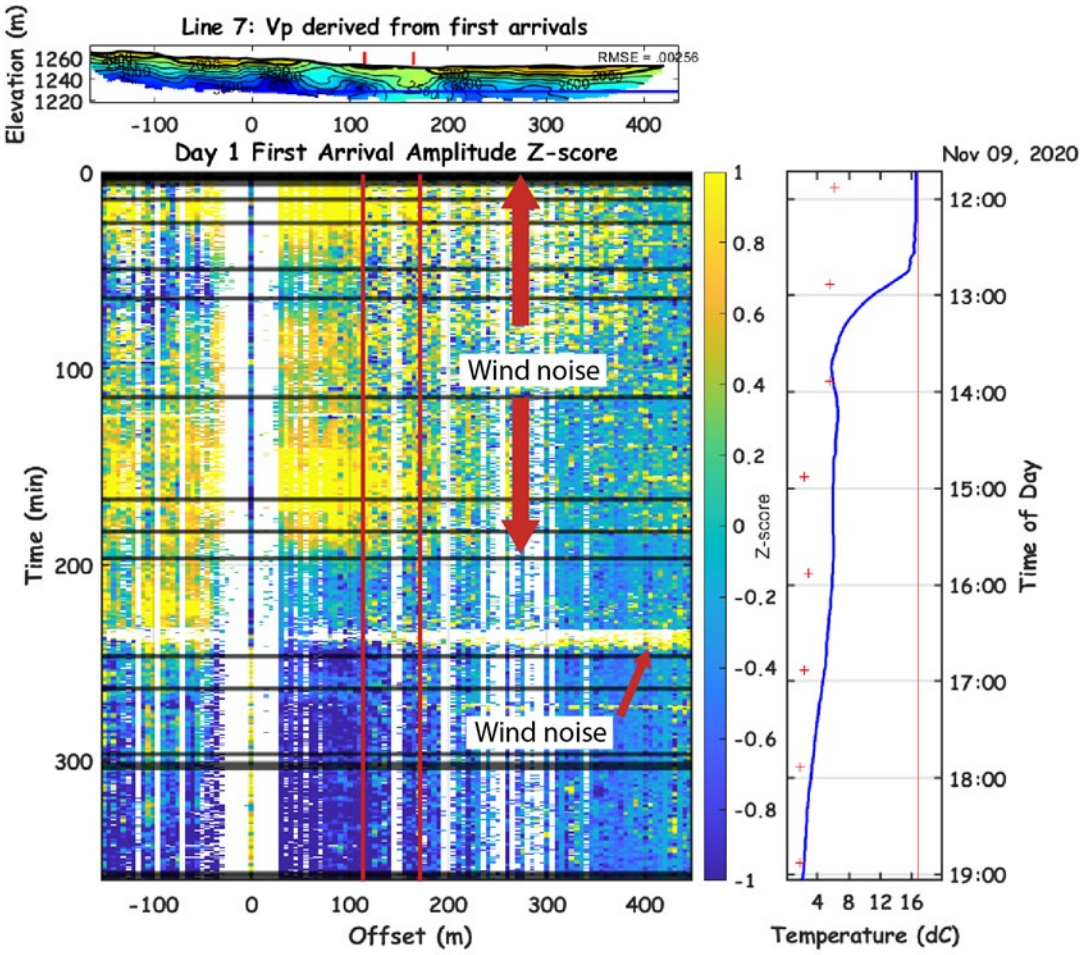

Figure 6.13 Top: Tomographic velocity model along line 7 by Yelton (2021) with red lines denoting fault zone. Center: first arrival amplitude Z-score during day one with back horizontal lines representing source skips/resets. Vertical red lines denote the fault zone identified by Yelton (2021). Right: Plot of transducer data for day one time lapse window.

Day 2

Time-lapse data for Day two data includes a 120-channel 10-second vertical geophone recordings acquired every thirty seconds between 08:09:29 and 17:45:18 MST on November 10, 2020 (Figure 6.13). I note that no eruptions occurred at Crystal Geyser during this window and the elevated transducer temperatures seen are likely radiative forcing (right panel Figure 6.13). For the first arrival travel times and amplitudes, I

observe a significant change in Z-score from 0-275 minutes. I speculate that this change is due to the characteristics of the source changing due to a slow increase of tilt of the hammering plate followed by an abrupt change when the plate was releveled. There are also recorded skips/resets where an abrupt change in Z-score happens during this window likely because of the releveling of the plate. I observe an increase in travel residuals that follow a similar pattern (Figure 6.14). This travel time shift can also be seen in the common offset gathers (Figure 6.10). I attribute this change to a reset of the source plate. Z-scores become more consistent at around 375 minutes, and I attribute this to the ground settling after the source was reset. I observe a localized high z-score that appears to slowly move from low to high offset during the 50-to-150-minute window. I speculate that this is due to human foot traffic along the array. I also observe the same high z-score bands that are seen in day one and attribute them to wind noise. Z-scores for reflectors A and C show similar noise z-score and travel time residual characteristics to the first arrivals (Figures 6.16 and 6.17). I note that reflectors and first arrivals gathered on day two do not show signs of change related to gas movement.

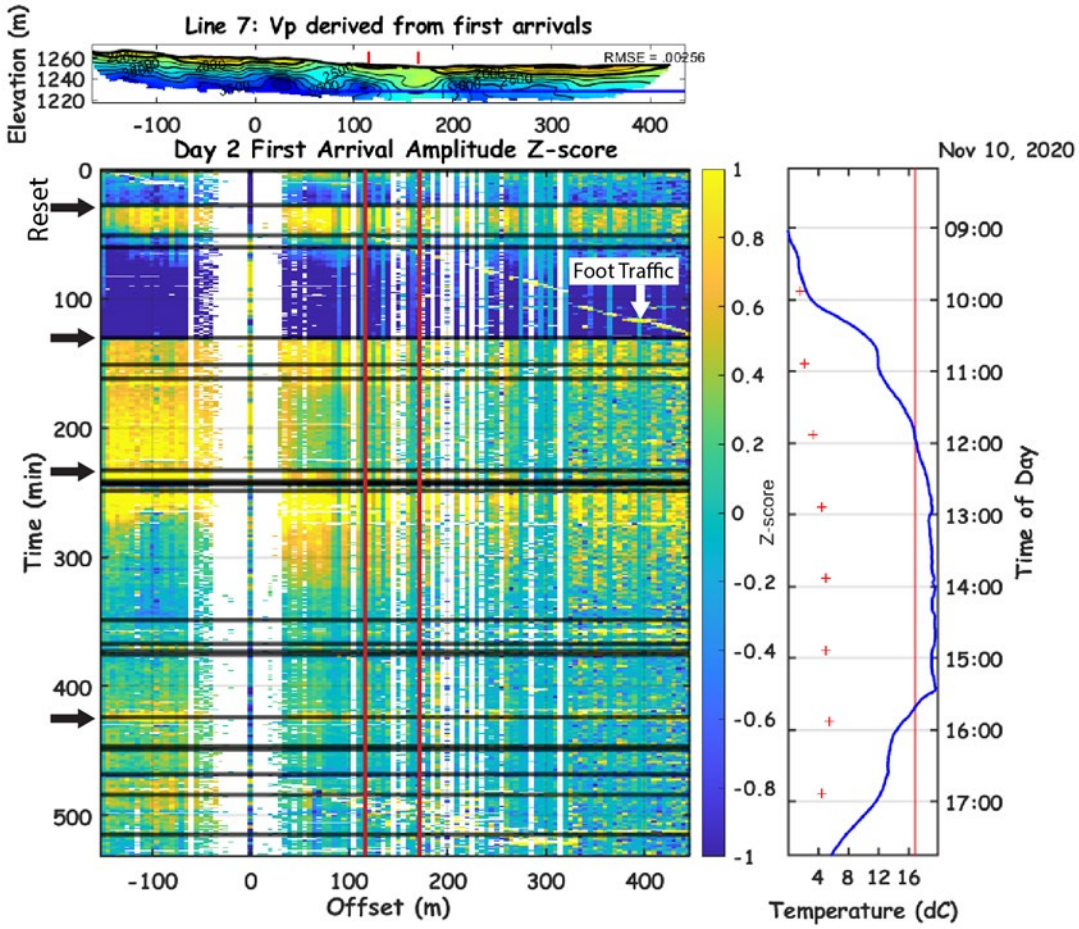

Figure 6.14 Top: Tomographic velocity model along line 7 by Yelton (2021) with red lines denoting fault zone. Center: Plot of first arrival amplitude Z-score during day two. Black horizontal lines represent source skips and black arrows on y-axis denote source resets. Vertical red lines denote the fault zone identified by Yelton (2021). Right: Plot of transducer data for day two timelapse window.

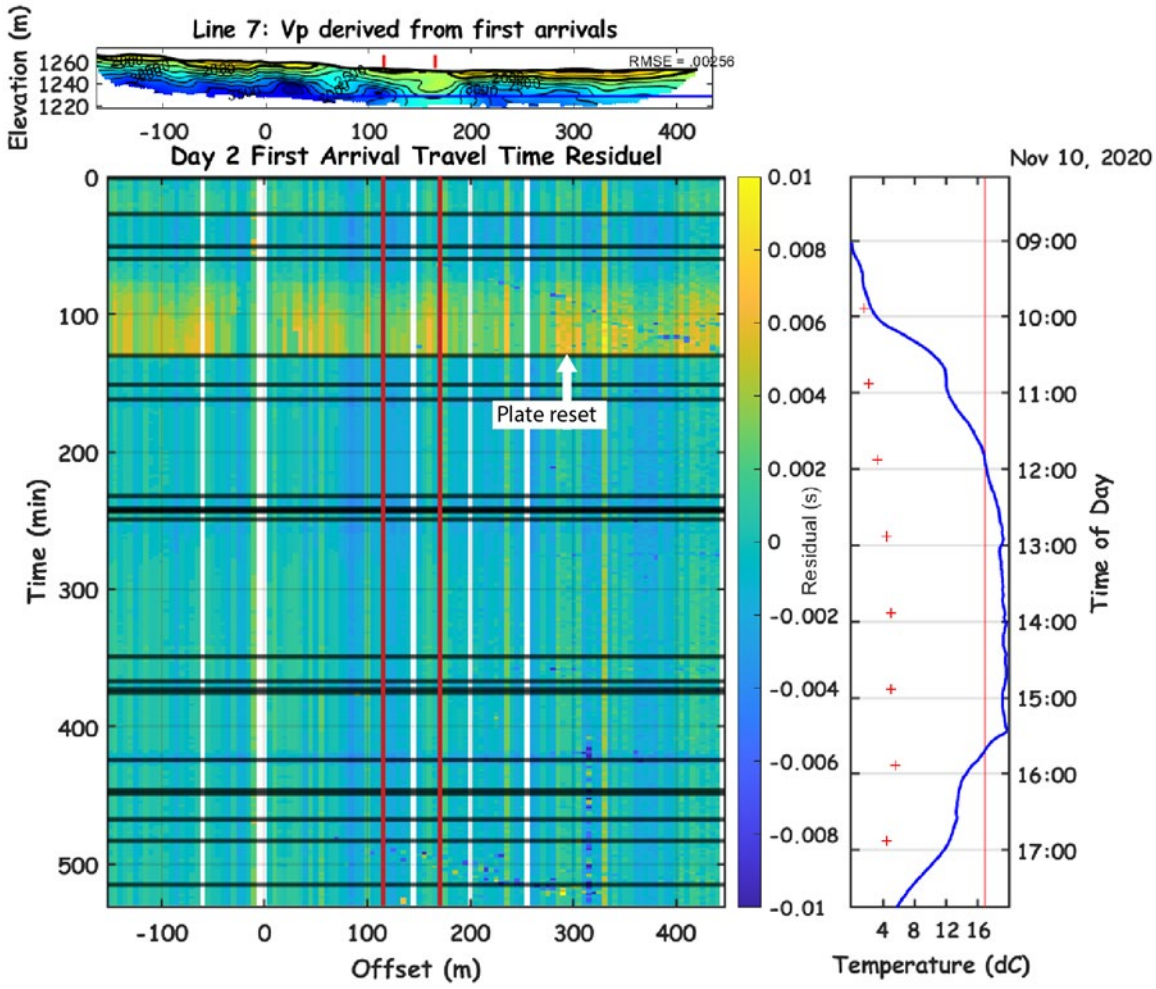

Figure 6.15 Top: Tomographic velocity model along line 7 by Yelton (2021) with red lines denoting fault zone. Center: Plot of first arrival travel time residual during day two with back horizontal lines representing source skips/resets. Right: Plot of transducer data for day two timelapse window. Vertical red lines denote the fault zone identified by Yelton (2021).

Day 3

Time-lapse data for Day three seismic data includes 120-channel 10-second vertical geophone recordings acquired every thirty seconds between 08:00:48 and 18:17:05 MST on November 11, 2020 (Figure 6.15). I note that a brief 30-minute eruption occurred at Crystal Geyser at 12:27 MST which was followed later by the start of a D-type eruption at 17:46 MST (right panel figure 6.15). For the first arrival travel

time and amplitude data, I observe abrupt changes in z-score at 200, 275 and 375 minutes followed by a period of elevated z-score. I attribute these to source resets as they all have corresponding source skips/resets that can also be seen in the common offset gathers (Figure 6.11). I also observe slight changes in travel time residuals with associated with each event. This change is likely due to a slight change in trigger timing as the source settles. The reflection data I observe during day three has the same z-score characteristics as the first arrivals (Figure 6.16 and 6.17). Reflection data I observe during day three show similar characteristics to the first arrivals and do not show evidence of changing amplitude signals through time related to gas saturation. Similar to Day 1 and Day 2, I also observe that reflector travel times and first arrivals do not show any significant change on day three. I note that reflectors and first arrivals gathered on day three do not show signs of change related to gas movement.

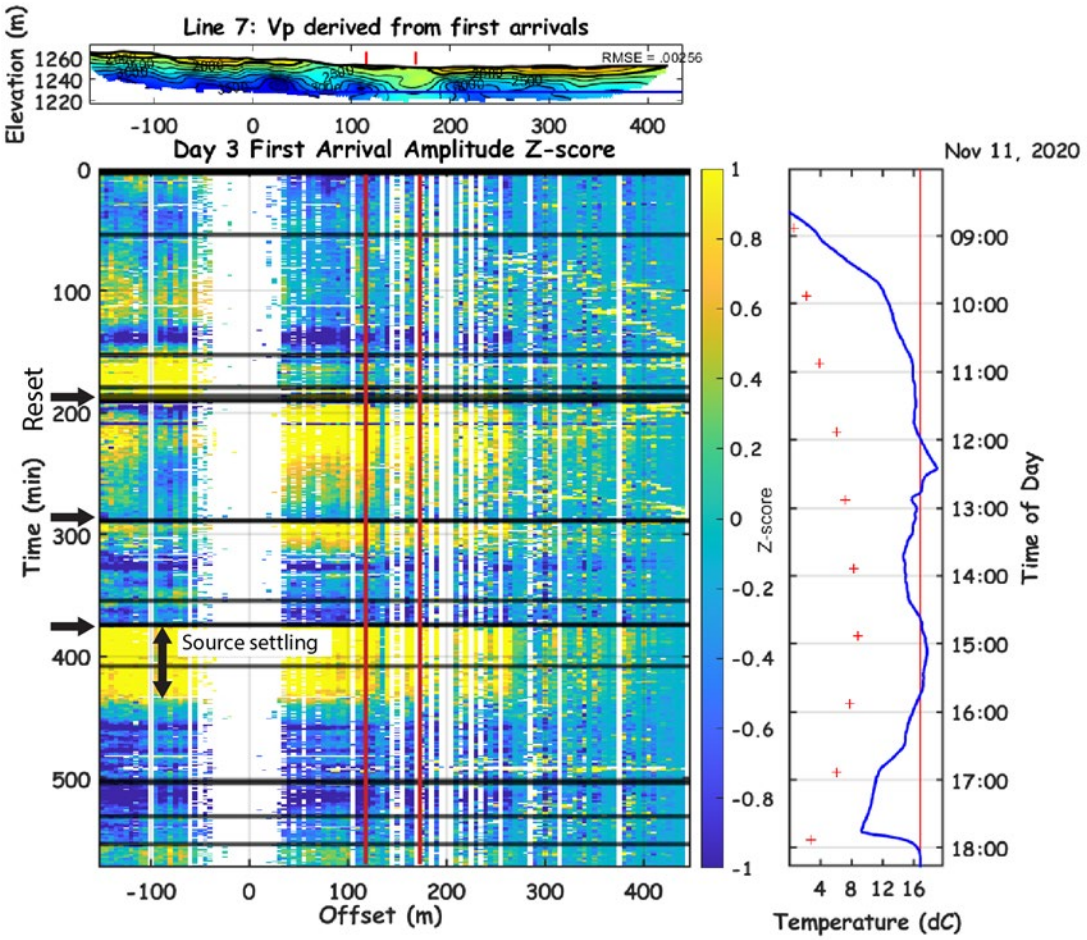

Figure 6.16 Top: Tomographic velocity model along line 7 by Yelton (2021). Center: Plot of first arrival amplitude Z-score during day three. Black horizontal lines representing source timing skips and black arrows are plate resets . Right: Plot of transducer data for day three timelapse window. Vertical red lines denote the fault zone identified by Yelton (2021). Left: A Crystal geyser eruption was recorded at 12:30 by the hunting camera at the peak temperature and a long-term D-type eruption begins just before 18:00.

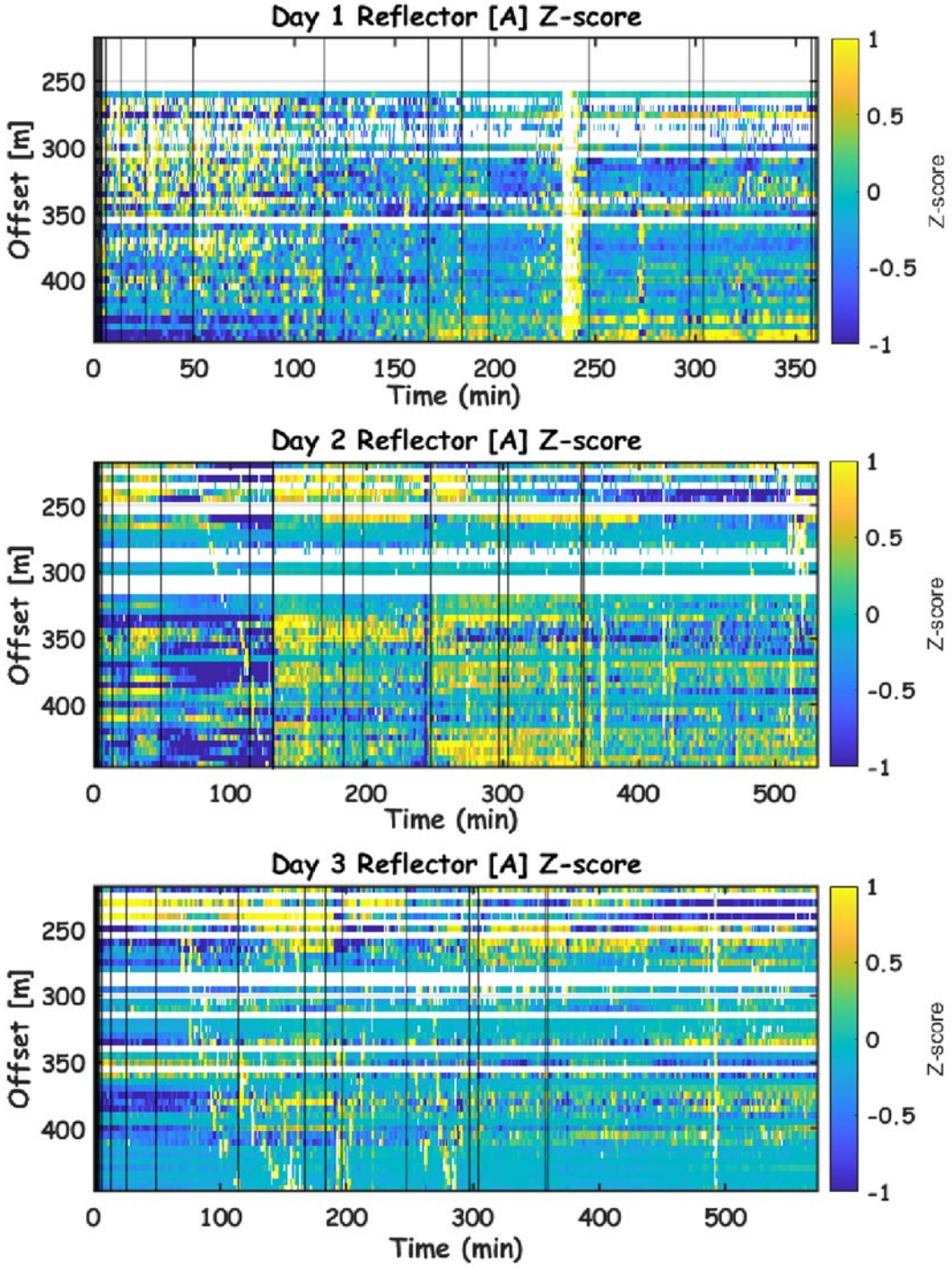

Figure 6.17 Z-scores for reflector "A" over all three days. Black vertical lines denote the skips/resets. White offsets were noisy or unable to be picked.

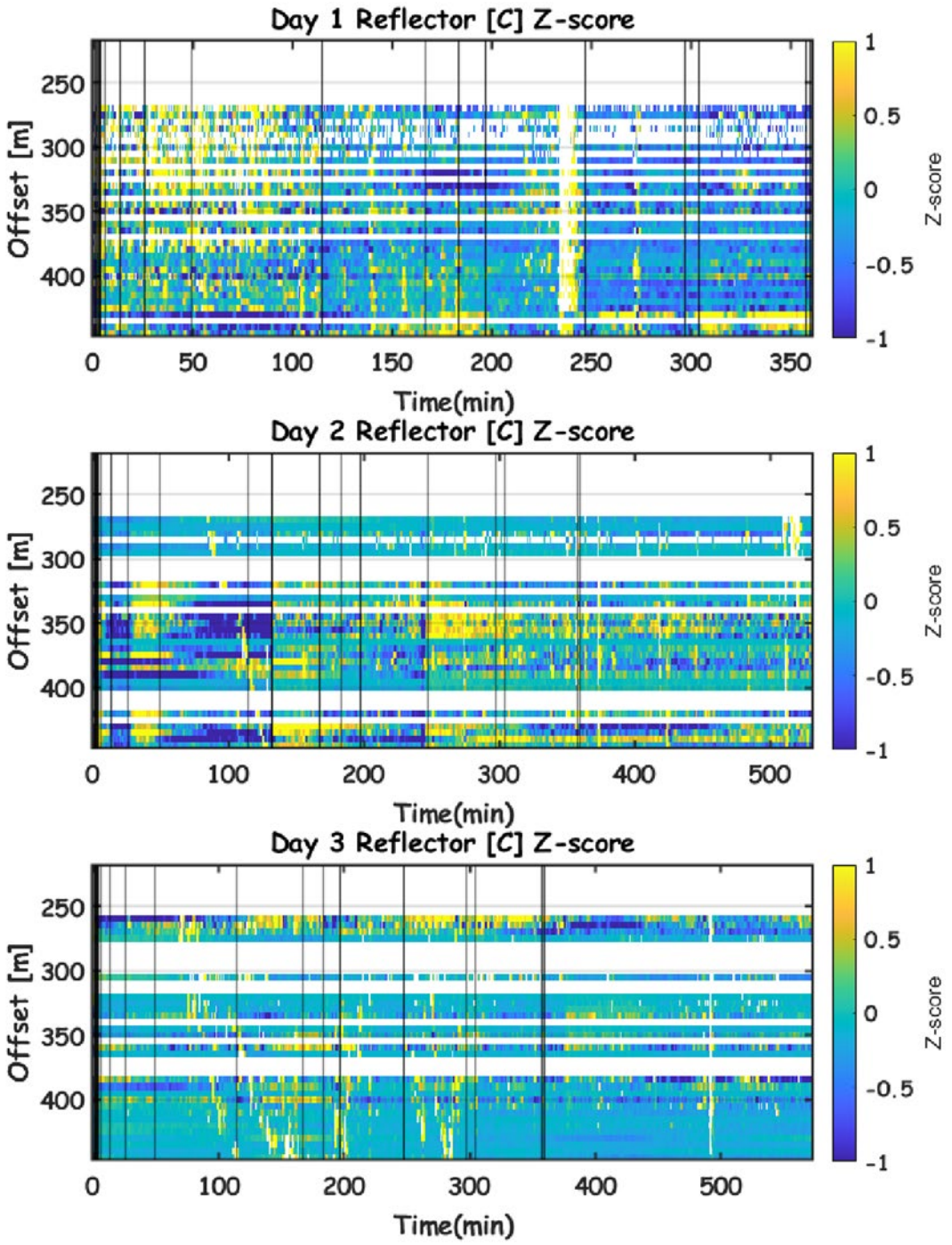

Figure 6.18 Z-scores for reflector "C" over all three days. Black vertical lines denote the skips/resets. White offset were noisy or unable to be picked.

Dispersion Analysis

Modeling by Jung et al. (2015) showed that gas saturations of up to 30% accumulated in the near surface of the hanging wall of the LGWF and within the fault. Surface waves are most sensitive to near-surface Vs structure. I hypothesize that as gas moves within the LGWF, pore pressure and water table elevation changes may change Rayleigh wave speeds. Additionally, I assess the Rayleigh wave repeatability from my seismic source across scales of minutes to hours to days.

I observe Rayleigh wave phase velocities from 550 to 750 m/s over a frequency range of 7-30 Hz within the hanging wall (Figure 6.19). I observe 1000-1400 m/s phase velocities from the geophones that lie above foot wall over a frequency range of 6-17 Hz (Figure 6.18).

To test for Rayleigh wave phase velocity continuity, I extract Rayleigh wave speeds along a high coherence frequency window (Figure 6.15) for the 30-hour time-lapse window. For the hanging wall data, I assess changing Rayleigh wave speeds between 14 and 15 Hz which probe about 25m in depth at observed speeds. I observe no measurable change in Rayleigh wave speeds on any day or between days (Figure 6.19). For the geophones located above footwall rocks, I extracted Rayleigh wave speeds between 9 to 10 Hz for the full 30-hour window. As with the hanging wall, I observe no change in Rayleigh wave speeds during the time-lapse measurements.

One factor that may cause a change in surface wave speed along Line 7 is a change in pore pressure or water table elevation with pulsing eruption cycles, as suggested by Jung et al. (2014). While Rayleigh waves are primarily composed of shear waves that are mostly insensitive to changes in fluids, the resulting change in density

from matrix saturation with water could cause a measurable change in Vs. For example, assuming a substrate that has a dry starting density of 1.85 g/cc, a Vs of 1000m/s and a gas filled porosity of 35%, it would experience a 10% Vs reduction after full water saturation or a difference of 100m/s. Changes at this scale could be resolved from this dataset. At a sampling frequency of 10Hz and Vs of 1000 m/s, I expect the greatest sensitivity within the upper 10's of meters. Assuming an unrealistic water table rise by 11m, the expected Vs may change to 957m/s or a 43m/s decrease. This end-member scenario may be hard to observe given the large phase velocity uncertainty of tens of meters/second.

This lack of Rayleigh wave speed change is consistent with Beaty & Schmitt (2003) who concluded that surface wave speeds were consistent in time with the use of a vibroseis source, even when taken across widely different soil harnesses and saturation states. As such, I conclude that my acquisition components were consistent through time and that no changing gas signal was measured through Rayleigh wave measurements.

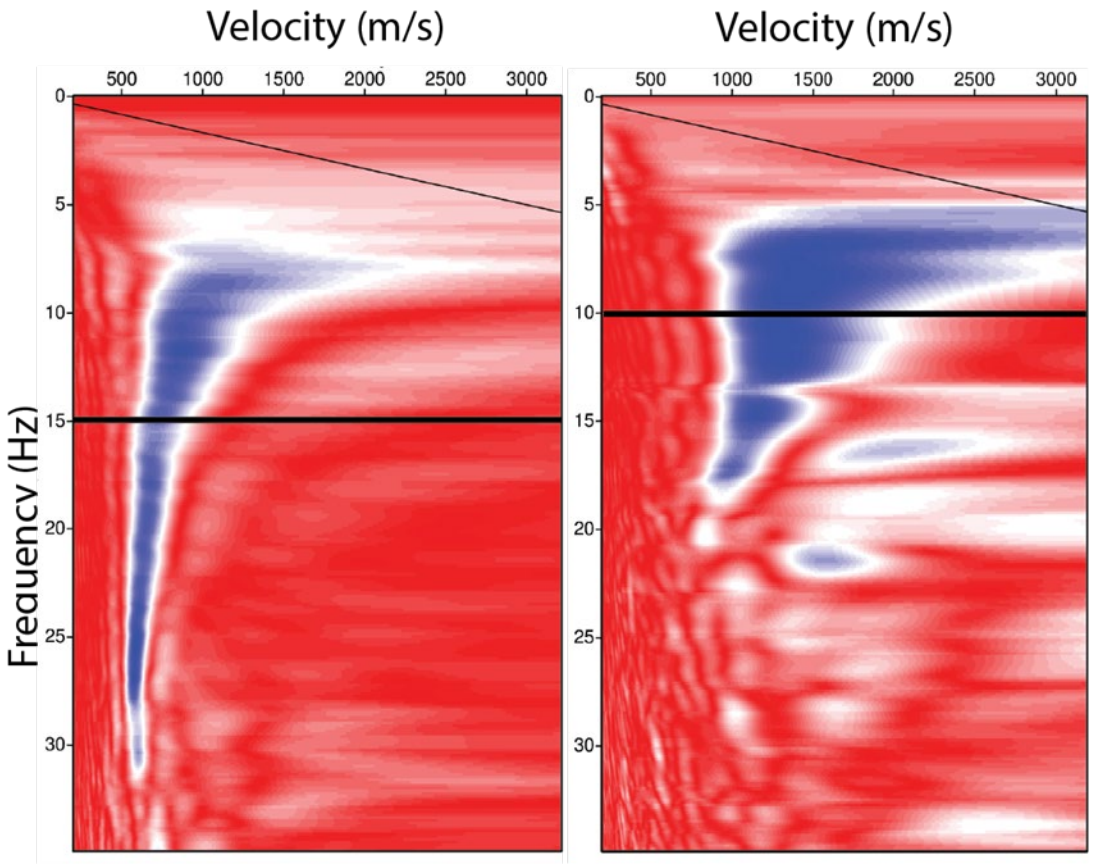

Figure 6.19 Dispersion curves of the first 5 shots on day two for the hanging wall (left) and the footwall (right) of the LGWF. Black lines denote frequencies examined over my time-lapse window in Figure (6.20)

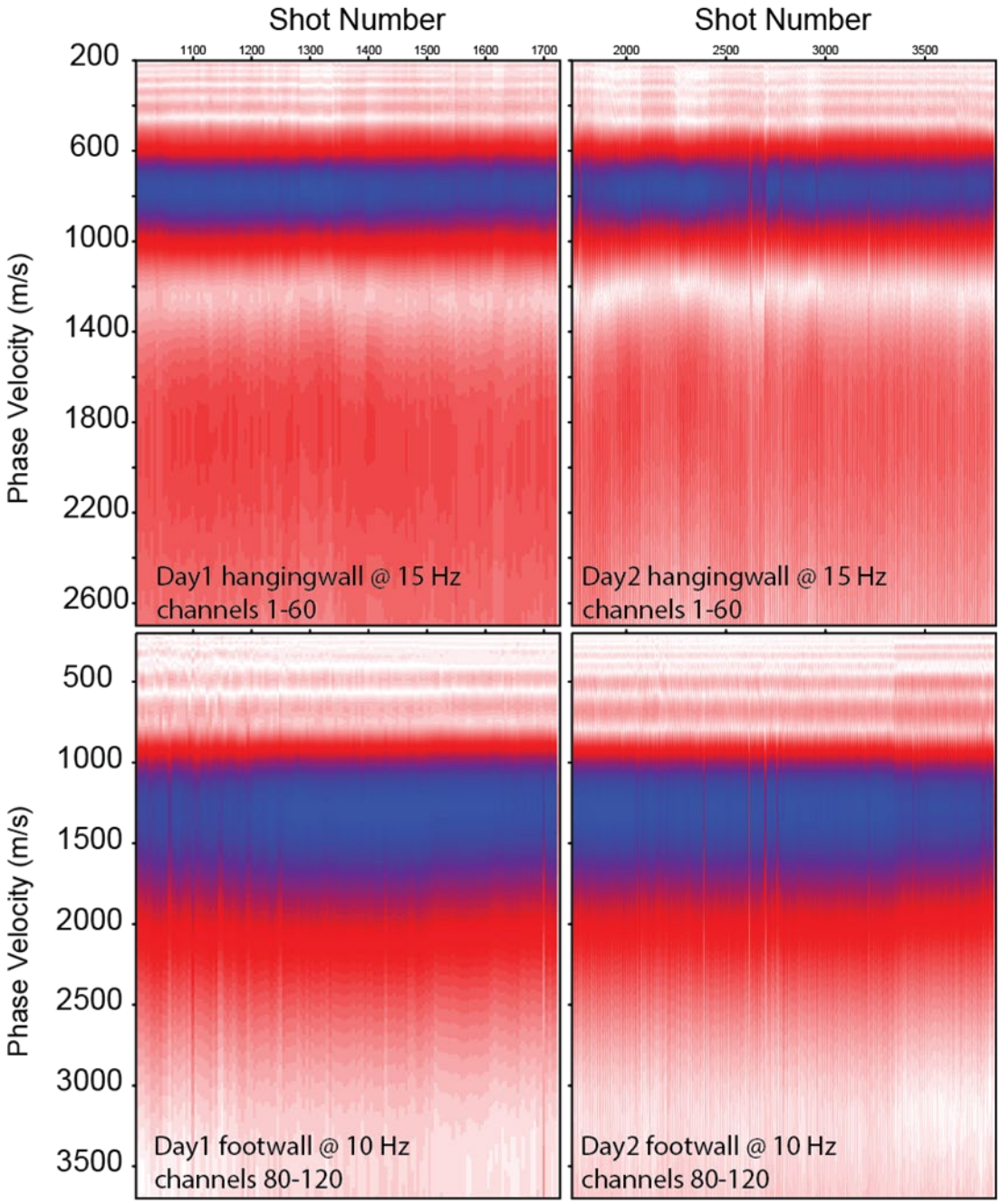

Figure 6.20 Dispersion curve time-lapse for 15 Hz (top) and 10 Hz (bottom) across Day one (left) and Day two (left).

CHAPTER SEVEN: DISCUSSION

My study tests a surface based seismic survey's ability to monitor changing saturation of CO_2 gas at reservoir and near surface depths. Here, I focus on Crystal Geyser eruption patterns, amplitude and travel time changes in the first arrivals and reflections in the time-lapse data, and the repeatability of surface wave data through time.

Previous recordings of the Crystal Geyser eruption cycles show decadal eruption pattern changes (Han et al., 2013; Kampman et al., 2014). I observe D-type eruption patterns and durations that differ from a previous study conducted by Kampman et al. (2014) in 2012. I observe that D-type eruption duration and time between events have both decreased when compared to the 2012 data set. However, I note that while this pattern is different than the one observed between Han et al. (2013) and Kampman et al. (2014), they show the same pattern the eruption duration increasing as a portion of the geyser cycle time. This suggests that Crystal Geyser's eruptions may progressively increase as a fraction of cycle time into the future. Additionally, Kelsey (1991) noted geyser eruptions in 1936 were 25 m to 45m in height which is much larger than present eruptions of 1-3 meters. I speculate based on historical accounts and the eruptions will diminish in vigor.

Modeling shows that a maximum Vp decrease of about 5.2% between 0 and 12% gas saturation. This would cause an observable change in both travel time and amplitude. However, changes in gas saturation above 20% result in amplitude and thus z-score changes that are less than what would be discernible qualitatively. This is because the

velocity changes at the higher saturations are smaller, and saturations would need a greater change to be observable. However, modeling does show that during the initial gas saturation of the reservoir seismic velocities would be observable. Thus, this method of monitoring may be better suited to new CCS sites during the initial CO_2 injection.

I observe no measurable change in Rayleigh wave speeds throughout the 30-hour time-lapse experiment. I observe no measurable change to either travel time or amplitude with in the first arrival or reflection data that would point to changing gas content with time. I speculate that the reason for this is mostly two-fold. (1) Gas saturation changes in the Navajo and Entrada reservoir range over saturation percentages that cause a limited change in Vp. (2) The outgassing seen at Line 7 is somewhat constant and does not go through measurable gas cycles like observed at the Crystal Geyser. I speculate the subsurface CO_2 in this area is in a steady state of equilibrium and does not change the saturation significantly enough to be measured seismically. This is supported by the models from Jung et al. (2015) which found that the Entrada and Navajo reservoirs could contain as much as 80% gaseous CO2 trapped against the LGWF. However, it is likely less than that upper bound as Kampman et al. (2014) did not find a gas cap within the Navajo reservoir to the west of the Crystal Geyser. This suggests a more moderate gas saturation. Both cases suggest that the reservoir is always at least partially saturated with CO2 which would mean change in subsurface velocity due to gas saturation would be limited.

Another factor to consider is unwanted noise in the data specifically source effects and wind noise which were prevalent in the data. Wind noise could be reduced if geophones were buried and would also increase repeatability(Schissele et al., 2009).

Source effects are primarily caused by excitation beyond the elastic limits of the soil and the type of source used (Pevzner et al., 2011, Aritman 2001). I speculate that source effects seen in my data set could be reduced if the material the hammering plate rests on is more competent and resistant to deformation such as concrete or asphalt or if a vibroseis source was used. As a result of not being able to observe seismic signals related to changing gas saturation along Line 7, I found no measurable relationship between Line 7 signals and eruptions at Crystal Geyser. This means that it is still unknown if an eruption at the geyser represents a local or regional CO_2 outgassing phenomenon.

I observe no significant changes in surface waves phase velocity across the data set. This suggests that the properties of the upper 60 meters of the subsurface are not measurably changing. Additionally, it should be noted that while body waves are sensitive to source effects, dispersion analysis of surface waves are insensitive to them. This is because this method only measures amplitude coherence at a given velocity and not absolute amplitude or timing.

Conclusion

Successful long-term storage of CO_2 requires subsurface monitoring to determine whether CO_2 is migrating. Ensuring that the CO_2 stays in the target reservoirs is crucial. I show that change in the Crystal Geyser's eruption time as a fraction of cycle is consistently increasing as it ages which suggests eruptions will get less vigorous. I show that modeling predicts that a maximum of 5.2% reduction in Vp speed is expected across low saturations of CO_2 gas which is measureable under noise-free acquisition conditions. However, no such changes are seen with in the seismic data, and this suggests either that

changes in gas saturations are not changing the velocity of either the reservoir rock or near-surface material enough to be observable or that they are obscured by source effects and noise. It is possible that while gas content is significant enough to reduce the Vp of the imaged materials by a significant amount, the amount it changes as degassing occurs is small and is unobservable. Being unable to observe changes in subsurface gas saturation also means I was not able to relate eruptions Crystal Geyser to changes subsurface gas along Line 7 two km to the east. Therefore, it is still unknown if the geyser represents a local CO_2 phenomenon or a regional pulse. I show that repeatability of surface and body waves is robust, but noise and source conditions can influence the seismic character.

My findings suggest that using surface based active source time-lapse to monitor the target reservoirs post CO_2 saturation may not be ideal as the velocity of the rocks will not change significantly after saturation beyond a certain threshold. Monitoring for CO_2 leaking into the overlying units from the target reservoir at a CCS maybe possible as the greatest change in Vp is expected at low gas percentages.

REFERENCES

Ajo-Franklin, J. B., Peterson, J., Doetsch, J., & Daley, T. M. (2013). High-resolution characterization of a CO2 plume using crosswell seismic tomography: Cranfield, MS, USA. *International Journal of Greenhouse Gas Control*, *18*, 497–509. https://doi.org/10.1016/j.ijggc.2012.12.018

Aritman, B. C. (n.d.). Repeatability study of seismic source signatures. In *GEOPHYSICS* (Vol. 66, Issue 6). http://pubs.geoscienceworld.org/geophysics/article-pdf/66/6/1811/3692902/gsgpy_66_6_1811.pdf

Baer, J.L., Rigby, J.K., 1978.Geology of the Crystal Geyser and environmental implications of its effluent, Grand County, Utah. Utah Geol. 5 (2).

Batzle, M., & Zhijing Wang. (1992). Seismic properties of pore fluids. Geophysics, 57(11), 1396–1408. https://doi.org/10.1190/1.1443207

Beaty, K. S., & Schmitt, D. R. (2003). Repeatability of multimode Rayleigh-wave dispersion studies. Geophysics, 68(3), 782–790. https://doi.org/10.1190/1.1581031

Boullenger, B., Verdel, A., Paap, B., Thorbecke, J., & Draganov, D. (2015). Studying CO2 storage with ambient-noise seismic interferometry: A combined numerical feasibility study and field-data example for Ketzin, Germany. Geophysics, 80(1), Q1–Q13. https://doi.org/10.1190/geo2014-0181.1

Burnside, N. M., Shipton, Z. K., Dockrill, B., & Ellam, R. M. (2013). Man-made versus natural CO2 leakage: A 400 k.y. History of an analogue for engineered geological storage of CO2. *Geology*, *41*(4), 471–474. https://doi.org/10.1130/G33738.1

Castagna, J. P., Batzle, M. L., & Eastwood, R. L. (1984). Relationships between compressional and shear-wave velocities in clastic silicate rocks. 1984 SEG Annual Meeting, SEG 1984, 50(4), 582–584. https://doi.org/10.1190/1.1894108

Dockrill, B., & Shipton, Z. K. (2010). Structural controls on leakage from a natural CO2 geologic storage site: Central Utah, U.S.A. *Journal of Structural Geology*, *32*(11), 1768–1782. https://doi.org/10.1016/j.jsg.2010.01.007

Doelling, H. H., Kuehne, P. A., Willis, G. C., & Ehler, J. B. (2015). Geologic map of the San Rafael Desert 30'x 60'quadrangle, Emery and Grand Counties, Utah. Utah Geological Survey.

E.S. Kerebes (1991). zoeppritz.m: Consortium for Research in Elastic Wave Exploration Seismology (CREWES) Toolbox Version: 2081

Felix Birkelbach (2022). Carbon dioxide thermodynamic properties (https://www.mathworks.com/matlabcentral/fileexchange/77512-carbon-dioxide-thermodynamic-properties), MATLAB Central File Exchange. Retrieved May 10, 2022.

Gassmann, F. (1951). ELASTIC WAVES THROUGH A PACKING OF SPHERES. GEOPHYSICS, 16(4), 673–685. https://doi.org/10.1190/1.1437718.

Han, W. S., Lu, M., Mcpherson, B. J., Keating, E. H., Moore, J., Park, E., Watson, Z. T., & Jung, N. H. (2013). Characteristics of CO2-driven cold-water geyser, Crystal Geyser in Utah: Experimental observation and mechanism analyses. *Geofluids*, *13*(3), 283–297. https://doi.org/10.1111/gfl.12018

Heath, J. E., Lachmar, T. E., Evans, J. P., Kolesar, P. T., & Williams, A. P. (2009). Hydrogeochemical characterization of leaking, carbon dioxide-charged fault zones in east-central utah, with implications for geologic carbon storage. *Geophysical Monograph Series*, *183*, 147–158. https://doi.org/10.1029/2006GM000407

Jenkins, C., Chadwick, A., & Hovorka, S. D. (2015). The state of the art in monitoring and verification - Ten years on. *International Journal of Greenhouse Gas Control*, *40*, 312–349. https://doi.org/10.1016/j.ijggc.2015.05.009

Jung, N. H., Han, W. S., Watson, Z. T., Graham, J. P., & Kim, K. Y. (2014). Fault-controlled CO2 leakage from natural reservoirs in the Colorado Plateau, East-

Central Utah. *Earth and Planetary Science Letters*, *403*, 358–367. https://doi.org/10.1016/j.epsl.2014.07.012

Jung, N., Han, W. S., Han, K., & Park, E. (2015). *Journal of Geophysical Research : Solid Earth*. 3003–3025. https://doi.org/10.1002/2014JB011722.Received

Kampman, N., Bickle, M. J., Maskell, A., Chapman, H. J., Evans, J. P., Purser, G., Zhou, Z., Schaller, M. F., Gattacceca, J. C., Bertier, P., Chen, F., Turchyn, A. v., Assayag, N., Rochelle, C., Ballentine, C. J., & Busch, A. (2014). Drilling and sampling a natural CO2 reservoir: Implications for fluid flow and CO2-fluid-rock reactions during CO2 migration through the overburden. *Chemical Geology*, *369*, 51–82. https://doi.org/10.1016/j.chemgeo.2013.11.015

Kelemen, P., Benson, S. M., Pilorgé, H., Psarras, P., & Wilcox, J. (2019b). An Overview of the Status and Challenges of CO2 Storage in Minerals and Geological Formations. *Frontiers in Climate*, *1*. https://doi.org/10.3389/fclim.2019.00009

Kelsey, M. R. (1991). River guide to canyonlands national park and vicinity: Featuring: Hiking, camping, geology, archaeology and steamboating, Cowboy, Ranching & Trail Building History. Kelsey Pub.

Kumar, Dhananjay. (2006). A Tutorial on Gassmann Fluid Substitution: Formulation, Algorithm and Matlab Code. Geohorizons. 4-12.

Lee, M. W. (2005). Proposed moduli of dry rock and their application to predicting elastic velocities of sandstones (Scientific Investigations Report 2005–5119; Version 1.0). doi:10.3133/sir20055119

Lemmon, E.W., McLinden, M.O., Friend, D.G., 2005. Thermophysical properties of fluid systems. In: Linstrom, P.J., Mallard, W.G. (Eds.), Chemistry Web Book. NIST Standard Reference Database Number 69, National Institute of Standards and Technology.

Lindsey, R. (2022). Climate change: Atmospheric carbon dioxide. Climate Change: Atmospheric Carbon Dioxide | NOAA Climate.gov. Retrieved July 23, 2022, from https://www.climate.gov/news-features/understanding-climate/climate-

change-atmospheric-carbon-dioxide Mavko, G., Mukerji, T., & Dvorkin, J. (2009). The Rock Physics Handbook: Tools for Seismic Analysis of Porous Media (2nd ed.). Cambridge: Cambridge University Press. doi:10.1017/CBO9780511626753

Lubbers J, Graaff R. A simple and accurate formula for the sound velocity in water. Ultrasound Med Biol. 1998 Sep;24(7):1065-8. doi: 10.1016/s0301-5629(98)00091-x. PMID: 9809641.

Mavko, G., Mukerji, T., & Dvorkin, J. (2009). The rock physics handbook: Tools for seismic analysis of porous media. Cambridge, UK: Cambridge University Press.

Mayo, A., Shrum, D., & Chidsey, T., Jr.(1991). Factors contributing to exsolving carbon dioxide in ground water systems in the Colorado Plateau, Utah. Utah Geological Association Publication, Vol. 19, p.335-341.

Naruk, S. J., Solum, J. G., Brandenburg, J. P., Origo, P., & Wolf, D. E. (2019). Effective stress constraints on vertical flow in fault zones: Learnings from natural CO2 reservoirs. *AAPG Bulletin*, *103*(8), 1979–2008. https://doi.org/10.1306/12181817393

Nuccio, V. F., Condon, S. M., & Huffman, A. C. (n.d.). *Burial and Thermal History of the Paradox Basin, Utah and Colorado, and Petroleum Potential of the Middle Pennsylvanian Paradox Formation EVOLUTION OF SEDIMENTARY BASINS-PARADOX BASIN*.

Oye, V., Anell, I. M., Braathen, A., Dichiarante, A. M., Evans, J. P., Hafner, A., Horne, E., Liberty, L. M., Midtkandal, I., Petrie, E., Sauvin, G., Skurtveit, E., Yelton, J., & Zuchuat, V. (2021). *Monitoring and imaging of active and passive CO 2 seepage patterns*. https://ssrn.com/abstract=3819197

Park, Choon & Miller, Richard & Xia, Jianghai. (1999). Multichannel analysis of surface waves (MASW). Geophysics. 64. 10.1190/1.1444590.

Pevzner, R., Shulakova, V., Kepic, A., & Urosevic, M. (2011). Repeatability analysis of land time-lapse seismic data: CO2CRC Otway pilot project case study.

Geophysical Prospecting, *59*(1), 66–77. https://doi.org/10.1111/j.1365-2478.2010.00907.x

Pinzon-Rincon, L., Lavoué, F., Mordret, A., Boué, P., Brenguier, F., Dales, P., Ben-Zion, Y., Vernon, F., Bean, C. J., & Hollis, D. (2021). Humming trains in seismology: An opportune source for probing the shallow crust. *Seismological Research Letters*, *92*(2 A), 623–635. https://doi.org/10.1785/0220200248

Probst, A. J., Ladd, B., Jarett, J. K., Geller-Mcgrath, D. E., Sieber, C. M. K., Emerson, J. B., Anantharaman, K., Thomas, B. C., Malmstrom, R. R., Stieglmeier, M., Klingl, A., Woyke, T., Ryan, M. C., & Banfield, J. F. (2018). Differential depth distribution of microbial function and putative symbionts through sediment-hosted aquifers in the deep terrestrial subsurface. *Nature Microbiology*, *3*(3), 328–336. https://doi.org/10.1038/s41564-017-0098-y

Rahman, F. A., Aziz, M. M. A., Saidur, R., Bakar, W. A. W. A., Hainin, M. R., Putrajaya, R., & Hassan, N. A. (2017). Pollution to solution: Capture and sequestration of carbon dioxide (CO2) and its utilization as a renewable energy source for a sustainable future. In *Renewable and Sustainable Energy Reviews* (Vol. 71, pp. 112–126). Elsevier Ltd. https://doi.org/10.1016/j.rser.2017.01.011

Schissele, E., Forgues, E., Echappé, J., Meunier, J., de Pelleggrs, O., & Hubans, C. (2009). Seismic repeatability - Is there a limit? *71st European Association of Geoscientists and Engineers Conference and Exhibition 2009: Balancing Global Resources. Incorporating SPE EUROPEC 2009*, *5*, 2737–2741. https://doi.org/10.3997/2214-4609.201400421

Shipton, Z. K., Evans, J. P., Kirschner, D., Kolesar, P. T., Williams, A. P., & Heath, J. (2004). Analysis of CO 2 leakage through "low-permeability" faults from natural reservoirs in the Colorado Plateau, east-central Utah. *Geological Society Special Publication*, *233*, 43–58. https://doi.org/10.1144/GSL.SP.2004.233.01.05

Smith, T. M., Sondergeld, C. H., & Rai, C. S. (2003). Gassmann fluid substitutions: A tutorial. Geophysics, 68(2), 430–440. https://doi.org/10.1190/1.1567211

Stockwell, J. W., & Cohen, J. K. (2008). *The New SU User's Manual*.

Stockton, S. L., & Balch, A. H. (1978). The UTILITY OF PETROLEUM SEISMIC EXPLORATION. DATA IN DELINEATING STRUCTURAL FEATURES. WITHIN SALT ANTICLINES. Open-File Report 78-591.

Utah Geological Survey, Robert Blackett (2012). Utah Temperature-Gradient Borehole. Utah Geological Survey, Southern Regional Office, 88 E. Fiddler Canyon Rd., Cedar City, UT 84721

White, J. E. (1975). COMPUTED SEISMIC SPEEDS AND ATTENUATION IN ROCKS WITH PARTIAL GAS SATURATION. Geophysics, 40(2), 224–232. https://doi.org/10.1190/1.1440520

Wilkinson, M., Gilfillan, S., Haszeldine, S., & Ballentine, C. J. (2009). Plumbing the Depths: testing natural tracers of subsurface CO2 origin and leakage, Utah, USA. In M. Grobe, J. C. Pashin, & R. L. Dodge (Eds.), Carbon dioxide sequestration in geological media - State of the science (Vol. 59, pp. 619). AAPG Studies in Geology.

Williams, G., & Chadwick, A. (2012). Quantitative seismic analysis of a thin layer of CO2 in the Sleipner injection plume. Geophysics, 77(6). https://doi.org/10.1190/geo2011-0449.1

Xia, J., Miller, R. D., & Park, C. B. (1999). Estimation of near-surface shear-wave velocity by inversion of Rayleigh waves. Geophysics, 64(3), 691-700.

Yelton, J. (2021). Seismic Imaging of Active and Ancient CO 2 Pathways in the Little Grand Wash Fault (Doctoral dissertation, Boise State University).Zhu, T., Ajo-Franklin, J., Daley, T. M., & Marone, C. (2019). Dynamics of geologic CO 2 storage and plume motion revealed by seismic coda waves. *Proceedings of the National Academy of Sciences of the United States of America*, *116*(7), 2464–2469. https://doi.org/10.1073/pnas.1810903116

Zoeppritz, Karl (1919). Erdbebenwellen VII. VIIb. Über Reflexion und Durchgang seismischer Wellen durch Unstetigkeitsflächen. Nachrichten von der Königlichen Gesellschaft der Wissenschaften zu Göttingen, Mathematisch-physikalische Klasse, 66-84.